TREBALL DE FI DE CARRERA

TITLE: Interferometric SAR data analysis and processing

DEGREE: Technical Telecommunication Engineering
Speciality: Telecommunication Systems

AUTHOR: Álvaro Fernández Salas

DIRECTOR: Michele Crosetto

SUPERVISOR: Jaume Piera Fernández

DATE: 20th January of 2005

TITLE: Interferometric SAR data analysis and processing

DEGREE: Technical Telecommunication Engineering
Speciality: Telecommunication Systems

AUTHOR: Álvaro Fernández Salas

DIRECTOR: Michele Crosetto

SUPERVISOR: Jaume Piera Fernández

DATE: 20th January of 2005

Overview

The differential Interferometric Synthetic Aperture Radar (DInSAR) is a remote sensing technique, which has improved very quickly in recent years. The main application of this technique is the accurate estimation and monitoring of land deformation.

The goal of this project is the processing and analysis of DInSAR data with an experimental procedure developed at the Institute of Geomatics (IG).

This document reviews the basic concepts of radar, SAR images and the DInSAR technique. Furthermore, it describes in detail the work done with the experimental DInSAR procedure of IG.

TÍTOL: Processat i anàlisis de dades interferomètriques SAR.

TITULACIÓ: Enginyeria tècnica de telecomunicacions, especialitat en sistemes de telecomunicació.

AUTOR: Álvaro Fernández Salas

DIRECTOR: Michele Crosetto

SUPERVISOR: Jaume Piera Fernández

DATA: 20 de January de 2005

Resum

L'interferometria diferencial de radars d'obertura sintètica (DInSAR), una tècnica de teledetecció, s'ha millorat molt ràpidament als últims anys. La principal aplicació d'aquesta tècnica es l'estimació tan precisa i la monitorització de la deformació del sòl.

L'objectiu d'aquest projecte és el processat i l'anàlisi de dades DInSAR amb el procediment experimental desenvolupat al *Institut de Geomàtica.*

Aquest document repassa els conceptes bàsics del radar, de les imatges SAR i de la tècnica DInSAR. A més, es descriu en detall el treball fet amb el procediment experimental del IG.

Dedico el treball a tota la gent de l'IG, pel seu tracte i afecte, però sobretot dedico l'esforç del meu projecte als meus pares, que han tingut plena confiança en mi durant tota la meva vida d'estudiant.

INDEX

INTRODUCTION

This project consists of a study based on interferometric differential SAR (DInSAR), explaining its concepts and applications for earth monitoring. This document reviews the deformation estimation method of IG, which is based on DInSAR techniques.

DInSAR provides land deformation maps, based on calculation of phase difference of two SAR images, which cover the same area but at different time acquisition. The ground deformation can be caused by earthquake, volcano eruption, miner exploitations, etc. It is important to know the magnitude of this land movement for many applications.

The document is divided in 3 parts:

- *BASIC CONCEPTS:* Introduction to radar, SAR systems, SAR image processing, interferometry and differential interferometry concepts.

- *COMPLETE PROCEDURE:* Study of the IG procedure for deformation estimation. In IG are received SAR images from ERS-1 and ERS-2 satellites, both of European Spatial Agency, and is necessary a complex procedure, using DInSAR, to estimate the real terrain movement. Also this procedure must minimize or reject some parameters, which are summed into SAR images, produced by atmosphere, spatial decorrelation, etc.

- *EXPERIMENTAL PART:* This is the most important part of the project. In this chapter is described a chain of simulated SAR images, which are sum of virtual deformation and other parameters. These images were used for posterior running of all programs of the IG procedure, in order to study the quality of the software.

CHAPTER 1. BASIC CONCEPTS

This chapter reviews some necessary concepts, as radar acquisition, SAR system and Interferometry applications & tools, for a fine compression of next chapters. There is a brief explication of basic issues; InSAR and DInSAR are based in those concepts.
The final objective of the project is the study of SAR images, and some process of these data. Also is essential the study of techniques such as InSAR and DINSAR. Objective of Interferometry is the earth monitoring, creating Digital Elevation Models (DMT's) and computing the ground deformation estimation of working zone.

1.1. Radar

Radar (radio detection and ranging) is an electronic tool used to detect objects, its position and/or its movement direction. Radar was created during The Second World War, by English developers for military purposes, around 1941. A radar system usually operates in the ultra-high-frequency (UHF) or microwave part of the radio-frequency (RF) spectrum (picture 1.1). Radar can track storm systems, because precipitation reflects electromagnetic fields.

Radar system has several applications. Radar has been used to measure distances to the moon, other planets, asteroids, and artificial satellites. From unmanned space probes, radar has been used to map Venus, whose surface is obscured at visible wavelengths by a thick layer of clouds. But most known application for general public is its use by law enforcement in determining the speeds of motor vehicles. This type of radar does not display the exact position of an object, but determines its radial speed vector from the *Doppler Effect*.

Radar system can be passive systems (only receiver mode) or active systems (receiver and transmission mode), as SONAR, LIDAR, SAR, etc.

Most radar systems determine position in two dimensions: azimuth and radius (distance). The display is in polar coordinates. An antenna transmits RF pulses at defined intervals. The delay between a transmitted pulse and the echo, or return pulse, determines the radial position of the plotted point(s) for each azimuth direction on the display. The greater the echo delay from a particular object in space, the farther from the display centre its point appears. The maximum range of a UHF or microwave radar system depends on the height of the antenna above average terrain, the topography of the surface in the region, the atmospheric conditions in the region, and in some cases the level of radio background noise.

Designation	Abbreviation	Frequencies	Free-space Wavelengths
Very Low Frequency	VLF	9 kHz - 30 kHz	33 km - 10 km
Low Frequency	LF	30 kHz - 300 kHz	10 km - 1 km
Medium Frequency	MF	300 kHz - 3 MHz	1 km - 100 m
High Frequency	HF	3 MHz - 30 MHz	100 m - 10 m
Very High Frequency	VHF	30 MHz - 300 MHz	10 m - 1 m
Ultra High Frequency	UHF	300 MHz - 3 GHz	1 m - 100 mm
Super High Frequency	SHF	3 GHz - 30 GHz	100 mm - 10 mm
Extremely High Frequency	EHF	30 GHz - 300 GHz	10 mm - 1 mm

Table 1.1. Radio-Frequency bands.

Inside of actives system there are 2 types, according to antenna aperture.

- Real aperture radar (RAR): Antenna length marks resolution. Have azimuth resolution determined by the antenna beam width, that it is proportional to the distance between the radar and the target. In RAR systems antenna length >> wavelength.

- Synthetic Aperture Radar (SAR): Have azimuth resolution independent of the distance between the antenna and the target. These systems use signal processing to synthesise an aperture that is hundreds of times longer than the actual antenna by operating on a sequence of signals recorded in the system memory.

  Generally, depending on the processing, resolutions achieved are of the order of 1-2 metres for airborne radars and 5-50 metres for spaceborne radars.

The most useful SAR spaceborne radars for deformation estimation and digital elevation model generation are ERS-1 and ERS-2. ERS-1 was created in 1992 (Toulouse) and ERS-2 in 1995 (Netherlands). Actually ERS-1 is off service.
ERS-2 is largely identical to ERS-1. The platform is based on the design of ERS-1. Here there is the ERS-1 specification and lower its picture.

Orbit	Type: Near-circular, polar, Sun-synchronous Altitude: 782 to 785 km Inclination: 98.52 deg. Period: About 100 minutes Orbits per day: 14.3 Repeat cycle: 3-day, 35-day and 176-day
Instruments	Active Microwave Instrument comprising a SAR (image and wave modes) and a Wind Scatter meter; a Radar Altimeter; an Along Track Scanning Radiometer; Precise Range and Range-rate Equipment; and Laser Retro-relectors
Mass	Total mass: 2157.4 Kg Total payload: 888.2 Kg Total platform: 1257.2 Kg Active Microwave Instrument: 325.8 Kg Radar Altimeter: 96.0 Kg Laser Retro-reflectors: 2.5 Kg
Electrical Power	Payload peak power: <=2600 W Payload permanent power: <=550 W Power supply voltage: 23-37 V On-board energy: 2650 WH max
Attitude and Orbital Control	Type: 3 Axes stabilised earth pointed Absolute rate errors: <=0.0015deg. Sec (3 sigma) Maximum errors: bias 0.11deg. (Pitch/roll) 0.21deg. (Yaw); harmonic and Random 0.03deg. (Pitch/roll) 0.07deg. (Yaw) Prediction accuracy: 30 m (radial), 15 m (cross), 1000 m (along) Orbit restitution: 5 m (radial), 15 m (cross) 60 m (along)
Data Handling	On-board computer: word length: 16 bits Payload memory capacity: 20 K words max Payload data exchange: OBDH type bus Number of payload users: redundant
Communications	Transponder: coherent S-band (2 kbit/s) Transmission power: 50 to 200 mW max Telemetry rate: 2048 bit/s Telecommand rate: 200 bit/s Data down link: - X-band (105 Mbit/s high rate link for AMI image mode) - X-band (15 Mbit/s low rate link for real-time and playback of LBR data) - on-board recorders provide 6.5 Gbits storage - S-band telemetry links for housekeeping data

Table 1.2. ERS-1 specification.

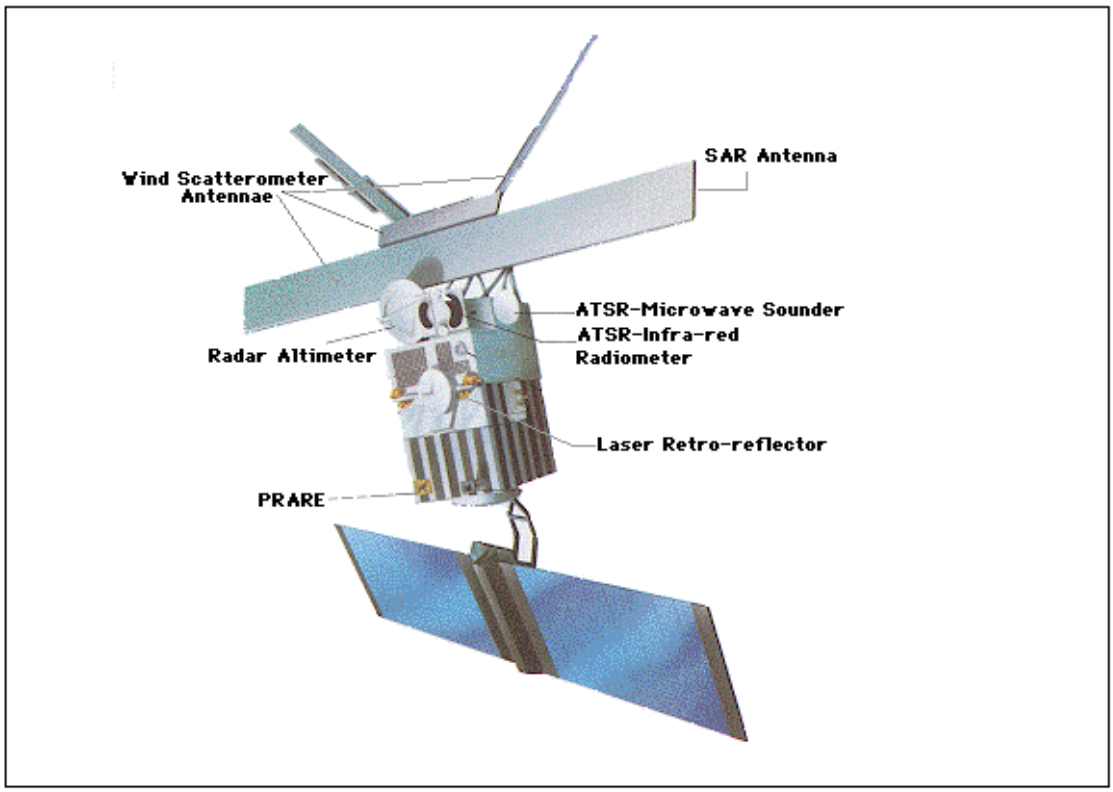

Fig.1.1. ERS-1 satellite picture.

1.2. SAR system

SAR is an image system. It is an active sensor transmitting and receiving microwave signals, i.e. measuring distances between the sensor and the point on the Earth's surface. This system is more complex than RAR; it requires more complex data processing but has a better resolution. SAR antennas are used in airborne and spatial systems.

Environmental monitoring, earth-resource mapping, and military systems require broad-area imaging at high resolutions. Many times the imagery must be acquired in inclement weather or during night as well as day. SAR can penetrate in terrain, snow and clouds… SAR systems take advantage of the long-range propagation characteristics of radar signals and the complex information processing capability of modern digital electronics to provide high resolution imagery.

SAR satellites usually send more than a thousand pulses toward the ground each second. However, since they are moving at around 7 kilometres per second, each pulse is 4 to 10 meters apart.

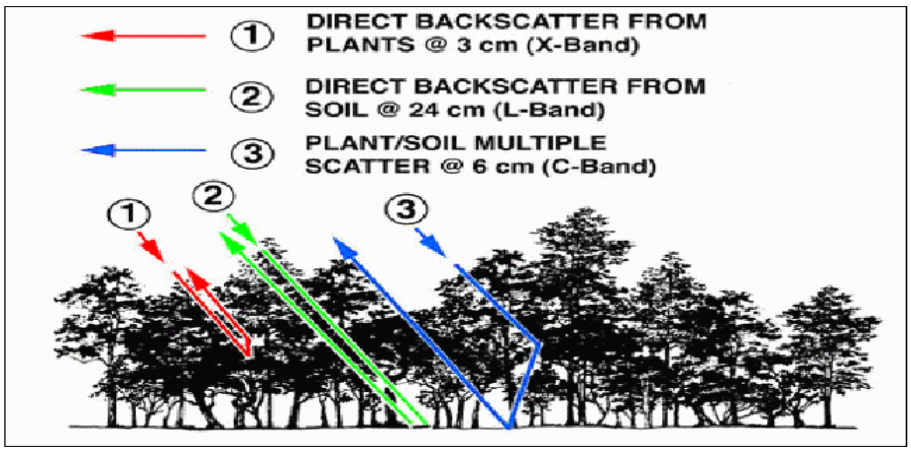

Fig.1.2. Different vegetation penetration.

There are different parameters in the receiving-transmition of SAR-data, which influence the data receiving:

a) Frequency: Waves have more or less penetration power depending on work frequency. The more wavelength, the more penetration power. See above picture.

b) Roughness surface: The Roughness of a surface depends on: wavelength, incidence angle and the superficies variability. A terrain is rough if its structure has similar dimensions than work wavelength.

c) Dielectric constant of surface: This property depends on materials humidity.

SAR technology has provided terrain structural information to geologists for mineral exploration, oil spill boundaries on water to environmentalists, sea state and ice hazard maps to navigators, and reconnaissance and targeting information to military operations.
SAR system use a technique based on antenna movement. The aim is use the movement of the antenna platform to provide a virtual antenna length, longer than real. This technique allow us obtain a higher accuracy in azimuth (satellite trajectory).

Typically, SAR produces a two-dimensional (2-D) image. One dimension is called range (or cross track) and is a measure of the "line-of-sight" distance from the radar to the target. SAR image columns are defined by the perpendicular direction respect platform (*slant range direction)*.

Range and azimuth are explained in next part. In the following picture can see them in an airborne system.

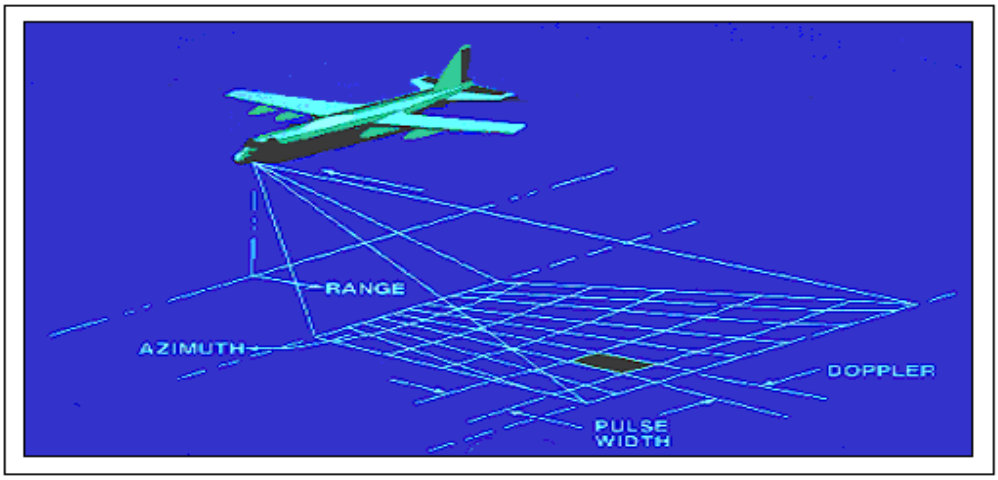

Fig.1.3. SAR system airborne.

1.2.1. Range resolution

Range is determined by precisely measuring the time from transmission of a pulse to receiving the echo from a target and, in the simplest SAR, range resolution is determined by the transmitted pulse width.

Two different target points illuminated by the radar beam reflect different series of echoes that can be distinguished in the return signal, if they are separated in time by at least the duration of the transmitted pulses. If the pulse duration is T_P, the slant range resolution limit (see figure 1.1) is then:

$$\Delta R_S = \frac{c \cdot T_P}{2} \qquad \textbf{(1.1)}$$

The resolution in ground range equals:

$$\Delta R_G = \frac{\Delta R_S}{\sin\Theta} = \frac{c \cdot T_P}{2 \cdot \sin\Theta} \qquad \textbf{(1.2)}$$

Where Θ is the SAR viewing angle (off-nadir angle). To obtain a reasonable resolution ΔR_G, the required pulse duration would be too short to deliver adequate energy per pulse. Therefore, to increase the echo signal to noise ratio (SNR) for reliable detection, a pulse compression technique is commonly employed. In this way, it is possible to achieve both high resolution (with longer pulse) and high SNR. The transmitted signal is linearly modulated in frequency

(chirp signal). With appropriate processing of the received pulse (matched filtering), the slant range resolution obtainable is:

$$\Delta R_S = \frac{c}{2 \cdot B_R} \qquad \textbf{(1.3)}$$

Where B_R is the frequency bandwidth of the transmitted pulse. The same resolution would be reached without pulse compression only using a very short pulse with duration $T_p = 1/B_R$. For instance, the slant range resolution of ERS-1/2 (less than 9 m) is obtained with pulse compression techniques using pulse duration of about 37 ms. The same resolution, without pulse compression, would require pulse duration of about 60 ns.

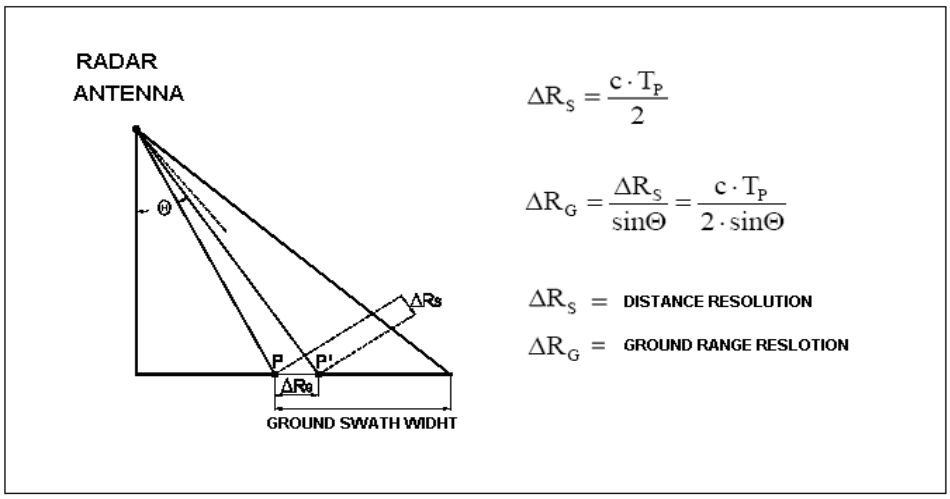

Fig.1.4. Radar system diagram.

1.2.2. Azimuth resolution

The other dimension is called azimuth (or along track) and is perpendicular to range. SAR image lines are defined by platform trajectory of antenna. It is the ability of SAR to produce relatively fine azimuth resolution that differentiates it from other radars. To obtain fine azimuth resolution, a physically large antenna is needed to focus the transmitted and received energy into a sharp beam. The sharpness (precision) of the beam defines the azimuth resolution.

The azimuth resolution of real aperture radars depends on the length L_A of the radar antenna in the flight direction (azimuth). The radar beam (i.e. the solid angle to which the transmitted EM energy is confined and from which the system can respond to the received signals) in azimuth direction is:

$$\Theta_H = \frac{\lambda}{L_A} \quad \textbf{(1.4)}$$

Where λ is the wavelength of the transmitted energy. Two target points laying on the ground at the same slant range R can be resolved, only if they are not both in the radar beam at the same time. The azimuth resolution limit is then:

$$\Delta Az = R \cdot \Theta_H = \frac{R \cdot \lambda}{L_A} \quad \textbf{(1.5)}$$

The longer the antenna length, the better the azimuth resolution. For spaceborne systems, the slant range distance being of several hundreds kilometres, an acceptable resolution (e.g. 10 m) requires an antenna length of many kilometres, which, of course, is impossible to realise. The concept of synthetic aperture provides high-resolution imagery, employing standard antenna length (e.g. 6-10 m). The key observation is that two point targets separated in azimuth at any time have different speeds relative to the platform. Therefore the radar pulse, when reflected from the two targets, has two distinct Doppler frequency shifts. Thus, even though the targets are at the same range and in the beam at the same time, they can be discriminated by analysis of the Doppler frequency spectrum of the return signal.

In order to synthesize the antenna length necessary to get a high resolution, all responses of a single target (in the time it remains in the radar beam) are used. Each signal sample contains the contributions of the different targets illuminated by the radar beam. The response of a given target is spread over many samples with different Doppler phase shifts, because the distance antenna-target is changing. Assuming the radar platform moving at speed v_S in a straight line at constant altitude (see figure 1.2), the distance antenna-target is a function of time:

$$R(t) = \sqrt{R_o^2 + Y^2(t)} = \sqrt{R_o^2 + (v_S \cdot t)^2} \quad \textbf{(1.6)}$$

Where R_o is the minimum radar-target distance and Y(t) is the antenna coordinate at time t.

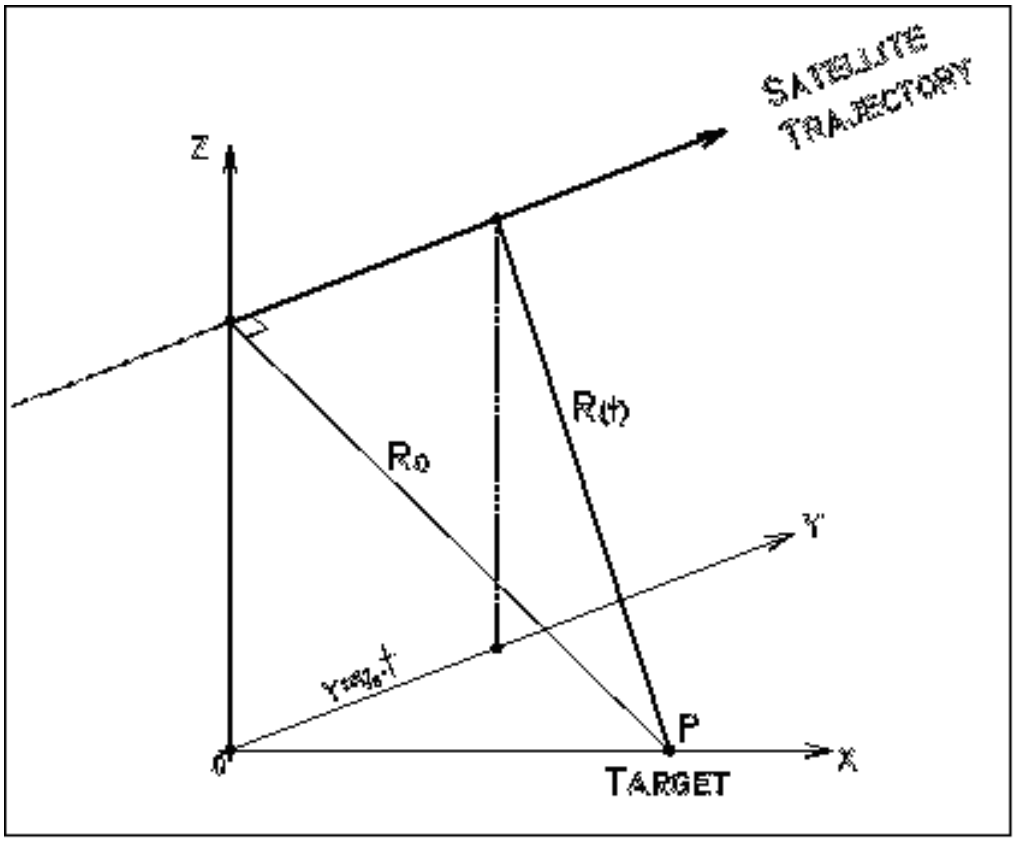

Fig.1.5. Antenna-target distance.

Since $Y = v_S \cdot t << R_o$,

$$R(t) \approx R_o + \frac{v_S^2 \cdot t^2}{2 \cdot R_o} \qquad \textbf{(1.7)}$$

The phase difference between transmitted and received waveforms due to the two-way travel over the range R is:

$$\Phi_s(t) = -\frac{4 \cdot \pi \cdot R(t)}{\lambda} \qquad \textbf{(1.8)}$$

The time derivative of $\Phi_s(t)$ is the Doppler frequency:

$$f_D = \frac{1}{2 \cdot \pi} \cdot \frac{d\Phi_s(t)}{dt} = -\frac{2 \cdot v_S^2 \cdot t}{\lambda \cdot R_o} \quad \textbf{(1.9)}$$

The change in Doppler frequency is linear with time. In order to achieve the full resolution, the data have to be collected over the interval I in which the target is in the radar beam:

$$I = \Theta_H \cdot R_o = \frac{\lambda \cdot R_o}{L_A} \quad \textbf{(1.10)}$$

To the interval I corresponds a Doppler bandwidth of:

$$B_D = \frac{2 \cdot v_S}{L_A} \quad \textbf{(1.11)}$$

The signal in azimuth can be treated in the same way as in slant range, i.e. by matched filtering. In this case the bandwidth of the compressed signal is the Doppler bandwidth B_D and the obtainable temporal resolution equals:

$$\Delta t_A = \frac{1}{B_D} = \frac{L_A}{2 \cdot v_S} \quad \textbf{(1.12)}$$

Hence, the spatial azimuth resolution is:

$$\Delta Az = v_S \cdot \Delta t_A = \frac{L_A}{2} \quad \textbf{(1.13)}$$

This is a very important result: the achievable azimuth resolution only depends on the antenna length L_A i.e. it is independent of the wavelength, the satellite speed and the satellite altitude. ΔAz has to be considered as a theoretical limit for the azimuth resolution; however, the resolution of current SAR's does approach this limit.

1.3. Focusing

The raw data have to undergo a sophisticated processing (called image compression or image focusing) in order to reach the high-resolution of the SAR images. All the usual SAR applications are based on compressed (focused) images. However, very often the users of SAR data are not directly concerned with the raw data and their relative processing.

Focusing is compression and filtering (in range and azimuth direction), the result are SLC image (Single Look complex). Also this function is called, processing, because it requires important resources of calculation. SLC images have real and imaginary part. In the following pictures we can see a focusing process; there are 2 compressions, one in azimuth direction, and another in range direction:

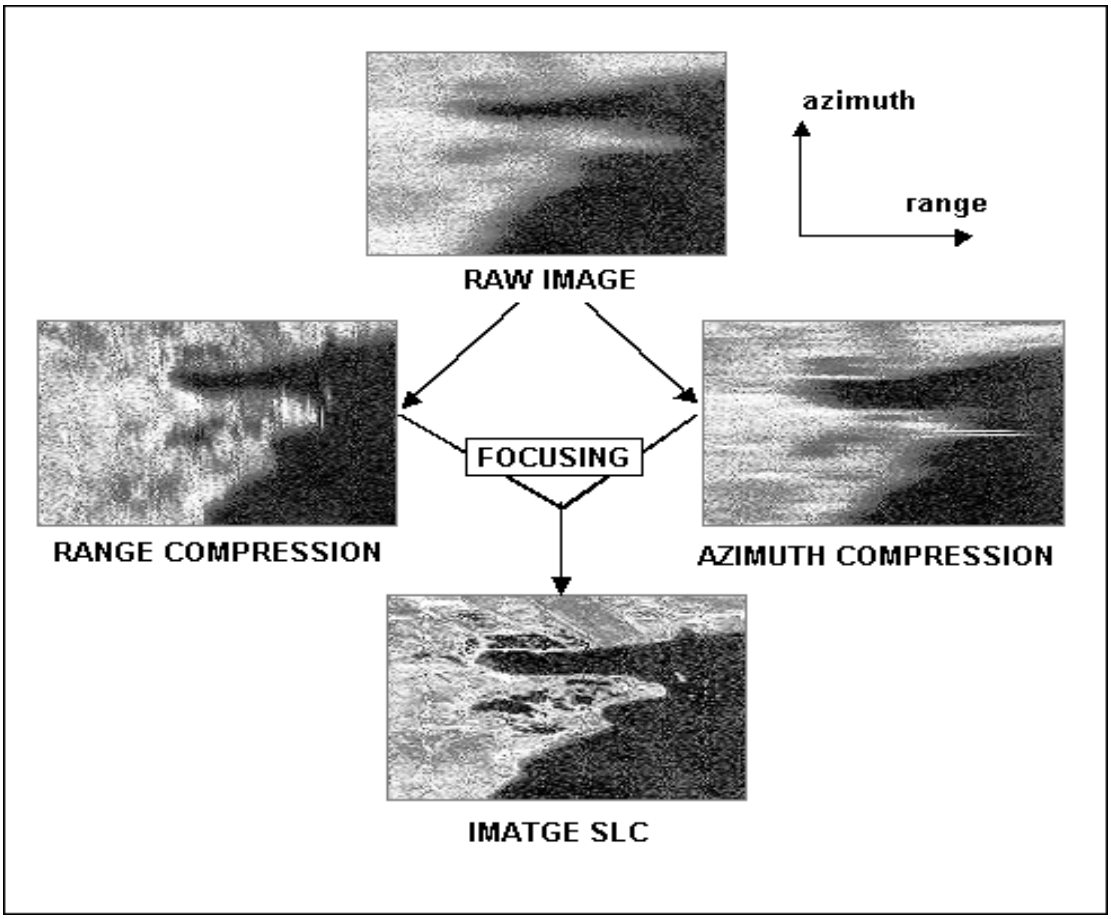

Fig.1.6. Focusing (Leucate-France-).

1.4. SAR image

A SAR image have complex information, each pixel is defined by a complex number, with real part and imaginary part.

Amplitude (real part): marks the reflexivity in caption image moment, if terrain surface has a good refraction amplitude is high. Then amplitude:

$$A = \sqrt{I^2 + Q^2} \qquad \textbf{(1.14)}$$

Where:

I is phase
Q is quadrature

The slant range nature of SAR data (due to the uniform sampling of the return signal) causes big distortion effects when mountainous or hilly terrain is imaged in the amplitude information.

The slant range nature of SAR data (due to the uniform sampling of the return signal) causes big distortion effects when mountainous or hilly terrain is imaged. There are four main distortion effects in amplitude, they are briefly described here:

Foreshortening: The slopes of mountains facing the antenna are shortened, i.e. appear compressed in the images (see segment 1-2 in figure 1.1). The reason of this compression can be easily understood in the extreme case when the slope elevation angle equals the radar beam off-nadir angle (i.e. the local incidence angle equals 90 degrees). In this case, all the points of the slope lie at the same slant range distance to the antenna so; even a mountain side few kilometres long is imaged in only one pixel. With a mitigated compression effect, the same applies to less inclined slopes

Layover: This is the extreme case to foreshortening, in which the top of a hill (mountain, etc.) is closer to the antenna than is its base (see segment 3-4 in figure 1.1). As a result, the echo from the top of the hill reaches the antenna before it receives the echo from the base. Because radar measures all distances with respect to time elapsed between transmission of a signal and the reception of its echo, the top of the hill appears in the image to be closer to the antenna than its base (thus inverting the local hill geometry).

Foreshortening and layover can be easily recognized because they appear very bright in the amplitude images. These two effects occur quite frequently in ERS SAR images because of the relative small viewing angle (the off-nadir angle is 23°) originally chosen for optimal sea surface observation and not for topographic applications.

Shadow: Another effect occurs on hill slopes, which are bent away from the look direction. Steep terrain may hide areas of the imaged scene from illumination by the radar beam, causing the so-called radar shadow. Such areas are not seen by the radar so no information about them is available (see segments 4-5 and 6-7 in figure 1.3).In this case, distances appear dilated in the images. This effect is just the opposite of the foreshortening one.

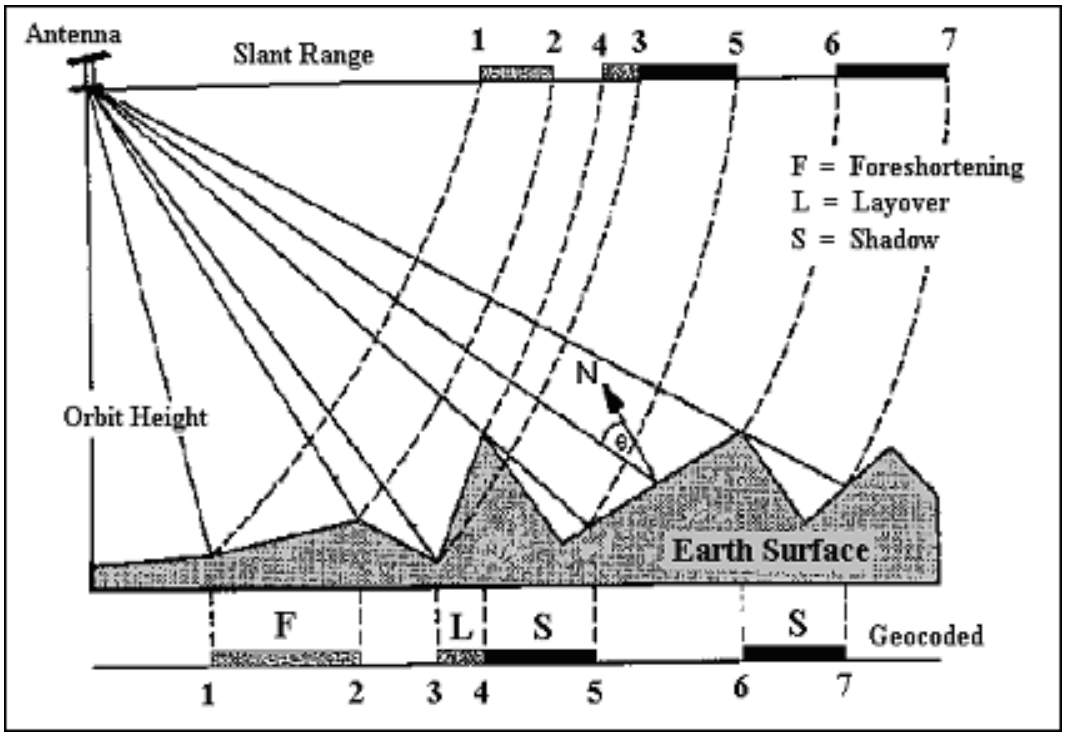

Fig.1.7. Geometric distortions of SAR image.

The combination of the three described effects makes the terrain sampling very irregular. The geometric distortions represent an inner limitation of the SAR system that affects both classical signal-amplitude-based and interferometric applications.

This distortion is obviously in following amplitude image of Barcelona. Collserola mountain range pictures some border or lines in right picture of fig.1.8.

Phase marks distance between caption point and ground. Distance is obtained in $\lambda/2$ module, that's why phase are wrapped, its value oscillate betweens $-\pi$ and π. Then phase:

$$\Phi = \tan^{-1}\left(\frac{Q}{I}\right) \qquad \textbf{(1.15)}$$

Where:

Q is quadrature
I is phase

SAR phase image is composed by:

- Phase movement caused by iteration of radar signal with ground. This parameter depends on dielectric constant and wave penetration power.
- Most important part of phase component is geometric phase (Φ_{geom}), Which marks the distance calculated between antenna and earth:

$$\Phi_{geom} = 2 \cdot \pi \cdot f_0 \cdot t = \frac{4 \cdot \pi \cdot R}{\lambda} \quad \textbf{(1.16)}$$

Where:

f_0 is carrier
λ is carrier wavelength
c is Light speed
R is distance (antenna-superficial point)

In Figure 1.8 can observe a phase image, it seems white noise. It is not useful for processing, because keeps an uniform distribution between $-\pi$ &π.

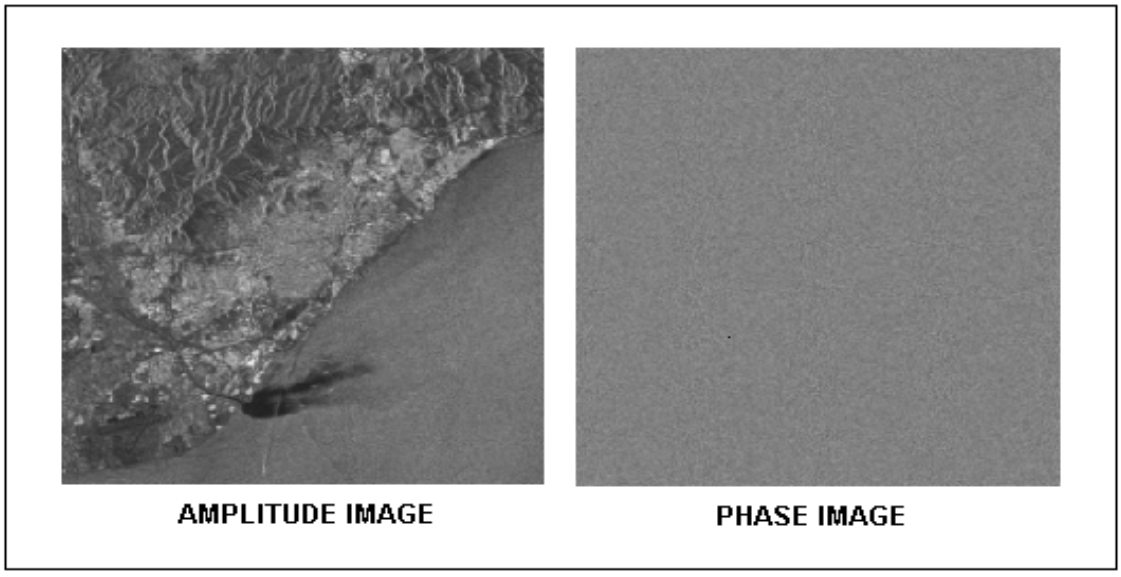

Fig.1.8. Amplitude SAR image and phase SAR image (Barcelona).

1.5. InSAR

From mapping the area coverage and magnitude of ground motions following cataclysmic earthquakes, to measuring discrete subsidence displacements over several years, InSAR has a wide variety of uses in ground movement surveying applications.

SAR interferometry makes use of this phase information by subtracting the phase value in one image from that of the other, for the same point on the ground. This is, in effect, generating the interference between the two phase signals and is the basis of interferometry.

The 2 images over same area are called master & slave. First acquisition is master and second is slave. After coregistration, we make difference between its phases (interferometric phase) ($\Delta\Phi_{Int}$):

$$\Delta\Phi_{Int} = \Phi_S - \Phi_M = \Phi_{Topo} + \Phi_{Mov} + \Phi_{Atm} + \Phi_{Noise} \quad \textbf{(1.16)}$$

Where:

Φ_{Topo} is phase difference cause of topographic distortion

Φ_{Mov} is phase difference cause of ground deformation

Φ_{Atm} is phase difference cause of atmospheric effects

Φ_{Noise} is phase difference cause of interferometric noise

There are 2 applications from this technique:

Digital Elevation Model (DEM) Generation: Is essential to have a null ground deformation between master and slave. With depreciable noise and atmosphere, topographic component give us terrain topographic.

Deformation estimation: Use DInSAR.

1.6. DInSAR

DInSAR allow to detect very accuracy ground deformation (a few mm) over wide areas. It's based on study and processing of SAR images. Final result of DINSAR is deformation map of working zone regards to a determined time.

For the deformation estimation, a phase component ($\Phi_{Topo\_simu)}$ is simulated from a previous knowledge of topography. Then it's possible the differential interferometric phase ($\Delta\Phi_{Int}$) calculation, it is based on interferometric phase, we take topographic component away from it.

$$\Delta\Phi_{D-Int} = \Delta\Phi_{Int} - \Delta\Phi_{Topo\_Simu} = \Phi_{Mov} + \Phi_{Atm} + \Phi_{Res\_Topo} + \Phi_{Noise} \quad \textbf{(1.17)}$$

Where:

Φ_{Mov} is phase difference cause of movement
Φ_{Atm} is phase difference cause of atmosphere
Φ_{Res_Topo} is phase difference cause of DEM errors
Φ_{Noise} is phase difference cause of phase noise

If linear-model is used, the result of DInSAR is a speed map, where the vertical movement is:

$$mov_v = \frac{\lambda \cdot \Phi_{Mov}}{4\pi \cdot \cos\theta} \quad \textbf{(1.18)}$$

Where:

λ is carrier wavelength
θ is the incidence angle
$\Phi_{\Delta Int}$ has a different sensibility regards to topographic and movement
Φ_{Topo} is function of base (master-slave):

$$\Phi_{Topo} = \frac{SP - MP}{\lambda / 4\pi} \quad \textbf{(1.19)}$$

SP is distance between satellite position (in the slave image acquisition moment) and surface point.
MP is distance between satellite position (in the master image acquisition moment) and surface point.

Φ_{Mov} is independent of base:

$$\Phi_{Mov} = \frac{SP^1 - SP}{\lambda / 4\pi} \quad \textbf{(1.20)}$$

SP^1 is distance between satellite position (in the slave image acquisition moment) and subsided surface point.

1.7. Baseline

In this section we comment a very important concept in SAR systems, baseline. Baseline is the distance between two satellites that can be represented by its length and its orientation, separated into two Cartesian components or expressed in polar form. The term "temporal baseline" refers to the time interval between successive satellite observations.

Sometimes in research application baseline is separated into two components, which can change (linearly) across an image. These are:

- Normal Baseline ($B_{\perp}$), the distance measured perpendicular to the centre look direction.
- Parallel Baseline ($B_{\parallel}$), the distance measured parallel to the centre look direction.

The baseline is used to interpret satellite phase as elevation. During DEM generation, the baseline must be known very accurately (within a few centimetres). As the baseline is rarely known this well beforehand, it needs to be refined using a reference DEM.

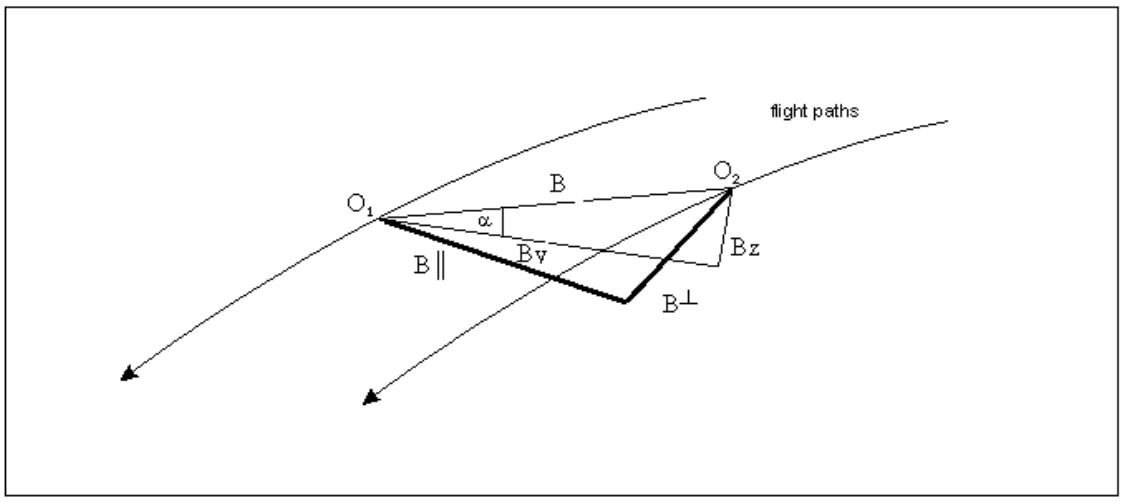

Fig.1.9. Representations of baseline.

1.8. Coregistration

In previous sections we have said that systems exploit the phase differences between two SAR images acquired over the same area, but always exists a spatial decorrelation (different orbits). It is necessary correlate these 2 SAR images. Normally decorrelation is in azimuth and slant range.

Coregistration typically has 2 steps:

- *Coarse coregistration* (Pixel level): Is a cross-correlation technique, utilise DFT (*Discrete Fourier Transform*) for compute the correlation peak.

- *Fine coregistration* (Sub-pixel level): Use automatic correlation techniques, interpolation tools and coherence. Compute the movement and transform slave image with regard to master image.

Figure 1.10 shows a pair of images (Master & Slave) that cover the same area, but exists a little spatial decorrelation, 7 lines in azimuth direction and 40 lines in range direction.

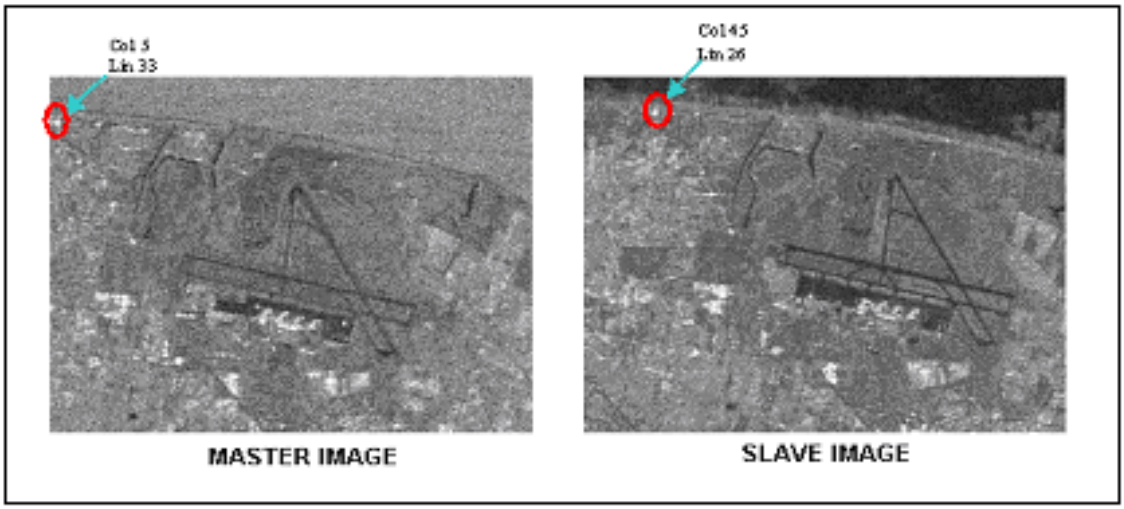

Fig.1.10. Slave image decorrelated regards to Master image. (Barcelona).

After coregistration, slave image is displaced. In figure 1.11 shows a null spatial decorrelation, some information is lost (blue colour):

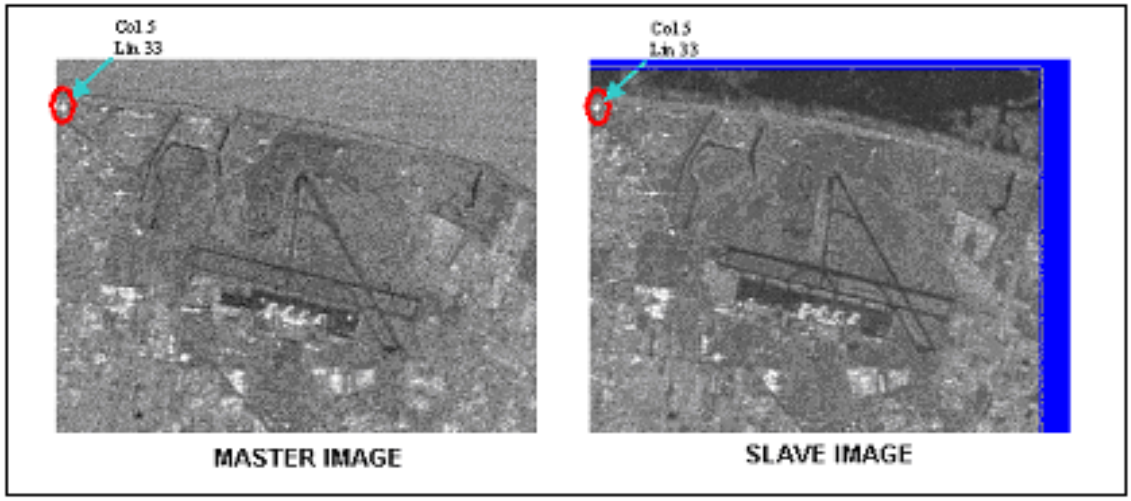

Fig.1.11. Slave image correlated regards to Master image. (Barcelona).

1.9. Interferogram

For generating an interferogram, two co-registered SAR images covering the same area are multiplied at this form:

$$INT_i = \mathrm{IMAGE}_{\mathrm{i\ Master}} \cdot (IMAGE_{i\ Slave})^* \quad \textbf{(1.21)}$$

Where:

INT_i is Interferogram *i*

$\mathrm{IMAGE}_{\mathrm{i\ Master}}$ is Master image *i*

$IMAGE_{i\ Slave}$ is Slave image *i*

$(IMAGE_{i\ Slave})^*$ is conjugated of $IMAGE_{i\ Slave}$

A master image is multiplied by its conjugated slave, or vice versa. INT_i module is the average of the two SAR images and INT_i phase is the difference of their corresponding phase values.

The phase of INT_i (Φ_{Int})is the sum of phases of nature effects (noise, atmosphere and movement) when we obtain Φ_{Mov} (movement), from Φ_{Int}, we have a slant range, but it is necessary computing the vertical movement.

1.10. Coherence

The coherence measures the degree of correlation between 2 images, and it is computed with following formula:

$$\gamma = \frac{\mathrm{E}\left[s_1 \cdot s_2^* \right]}{\sqrt{\mathrm{E}\left[|s_1|^2 \right] \cdot \mathrm{E}\left[|s_2|^2 \right]}} \quad \textbf{(1.22)}$$

Where:

s_1 is a SAR image

$s_1\, s_1\, s_2$ is a SAR image, covers same area than s_1 but decorrelated in time domain

s_2^* is conjugated of s_2

$E[\ ]$ is mean function

The coherence is a measure for the correlation of the phase information of two corresponding signals and varies in the range of 0 to 1. The degree of coherence can be used as a quality measure because it significantly influences the accuracy of phase differences and height measurements. Bright areas indicate regions of high coherence, whereas dark areas represent low coherence regions.

There are several factors decreasing the coherence. In approximate order:
Local slope (steep slopes lead to low coherence)

- Properties of the surface being imaged (vegetated or moving surfaces have low coherence).
- Time difference between the passes in an interferogram (long time difference lead to low coherence)
- The baseline (large baselines lead to low coherence)
- Technical details of the generation of the interferogram (poor coregistration or resampling leads to low coherence)

In the following picture it's possible to see how, the more temporal base, the less coherence. Also it's clear that urban zone have much more coherence than natural zones. White zones represent high coherence, black zone low coherence. Wood areas with temporal base of 1 day (figure 1.12.) can have medium of high coherence but after 35 days (figure 1.13.) will have poor coherence, that is sure.

Fig.1.12. Coherence image (Temporal base: 1 day).

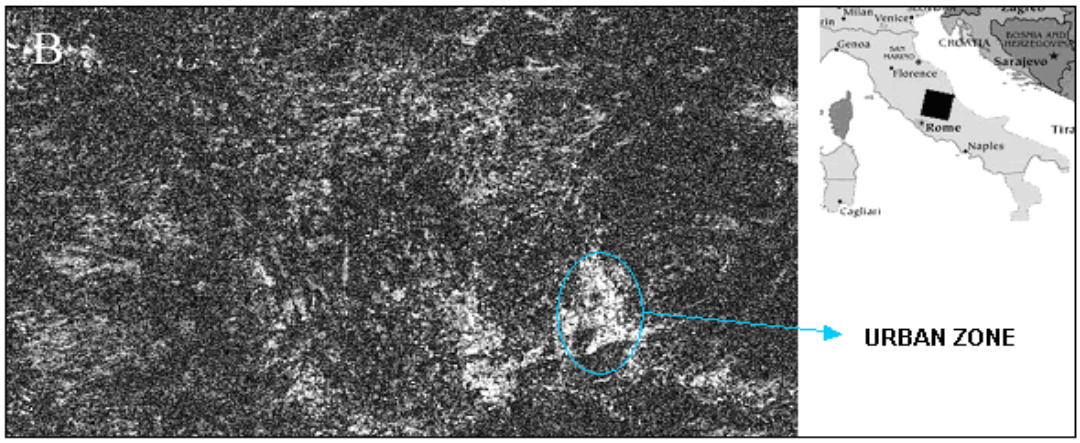

Fig.1.13. Coherence image (Temporal base: 35 days).

1.11. Phase Unwrapping

Radar only can detect phase between -Π and Π, because interferometric phase (Ψ) is result of quadrature (Q) and phase (I) of signal.
Phase unwrapping is the process of reconstructing the original phase shift from this "wrapped" representation. It consists of adding or subtracting multiples of 2Π in the appropriate places to make the phase image as smooth as possible. To convert interferometric phase into elevation, you must perform phase unwrapping.

Phase unwrapping is easy to do in areas of high coherence. Where decorrelation or layover contaminates the phase, it can be very difficult to extract topography accurately.

Often, phase unwrapping algorithms leave "holes", where they cannot determine the actual phase. They produce errors, where the unwrapped phase is (sometimes extremely) inaccurate.

There are different systems for unwrapping, such as:

- *Residue-cut*: Also called branch-cut, ghost-lines or minimum spanning tree.
- *Least squares* (LS): Based in the least squares.
- *Minimum cost flow* (MCF): Created by Constantini (1996). Based in flows over nets. This is the unwrapped method used in *Institute of Geomàtica*, is explained more ahead.

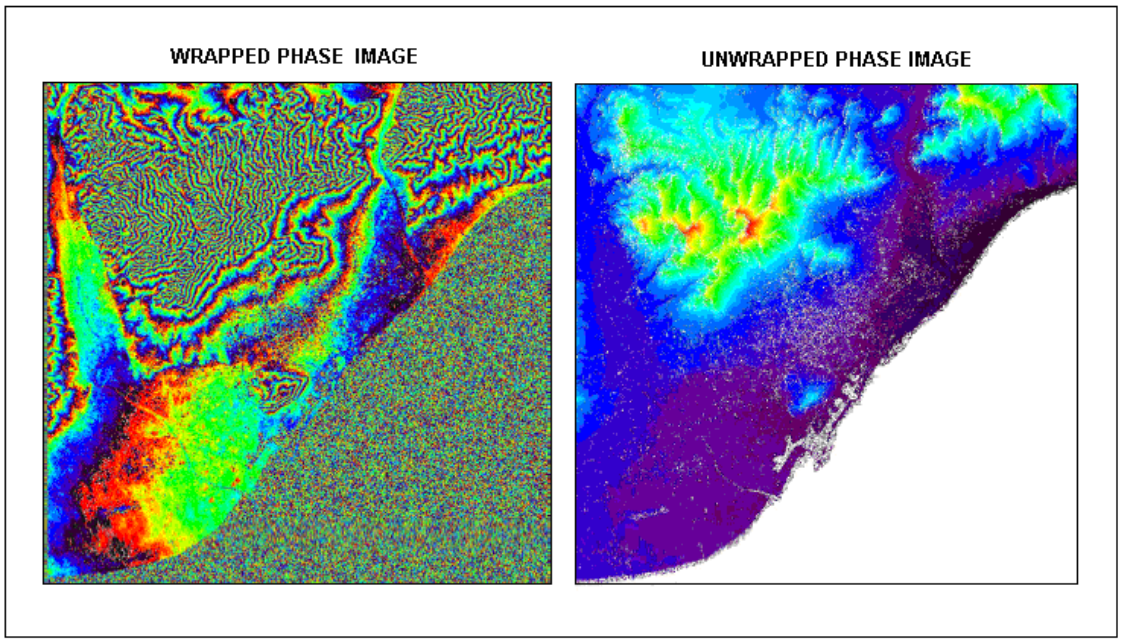

Fig.1.14. Wrapped and Unwrapped (coherence>0.3 & ΔT=1 day) phase images (Barcelona).

CHAPTER 2. COMPLETE PROCEDURE

Chapter 1 makes a theoretical explication of SAR procedures, applications, etc. In chapter 2 is described the procedure of IG, where from SAR complex images, the ground deformation is obtained. This is a procedure, which is one of possible procedures for deformation estimation. In next sections are explained all steps of this procedure.

The DInSAR procedure implemented by IG requires the following main input data:

- M SLC SAR images acquired over the area of interest. Note that the images must be suitable to form interferometric pairs, i.e. their spatial separation has to be typically of the order of few hundred meters.
- Stable area, marks the reference zone (non-subsidence).
- Working zone, describes what area will be considered.
- N coherence images, one for each interferogram. The coherence is a good indicator of the quality of the DInSAR phase: only the pixels characterized by good coherence (above a given threshold) are considered in the processing.
- Coherence threshold, marks limit between useful and useless points.
- Auxiliary data, which describe the main characteristics of the interferograms: master image (M), slave image (S), time separation between the two images (ΔT), perpendicular baseline ($B_{\perp}$), etc.
- Auxiliary data, which describe the SAR images: image dimensions, acquisition date, etc.

The outputs of the procedure include:

- The temporal evolution of the deformation for each selected pixel. The deformation is estimated in correspondence to each acquisition date of the SAR images. The date of the oldest image is chosen as temporal reference, i.e. the estimated values are relative deformation with respect to this date. The estimated deformation includes both the linear and non linear components of the deformation.
- The atmospheric contribution for each SAR image.
- The residuals of the different estimations, used to assess the quality of each step of the procedure.

In the following scheme can see all this procedure:

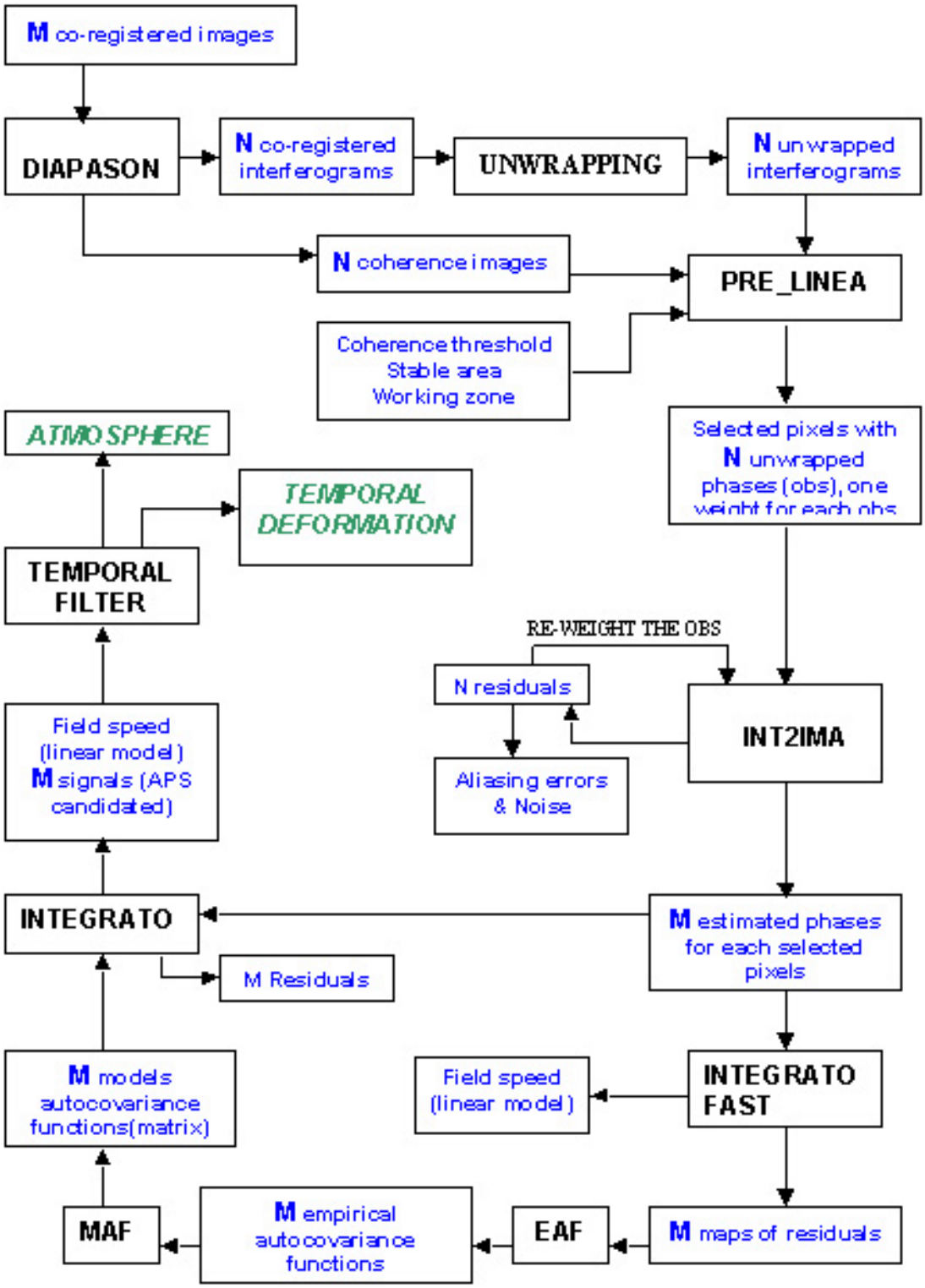

Fig.2.1. Procedure Scheme.

All these programs are described low:

Procedure explications:

- DIAPASON: Creates N interferograms. Makes an interferometric network from M SLC SAR images. Network Design can be modified by user. Also it creates N coherence images from interferometric phase.
- UNWRAPPING: Unwraps the N interferograms.
- PRE-LINEA: Marks the working zone, picks fine pixels considering the coherence threshold. Gives null value to all stable area pixels.
- INT2IMA: Builds M estimated phases for each selected pixels though this procedure (twice):
    - Puts the phases of the first image equal to zero.
    - The rest of images are referred to the first one.
    - Computes residuals and take away aliasing errors during second iteration.
- INTEGRATO FAST: Makes M maps of residuals and a field speed.
- EAF & MAF: Empirical and Model Autocovariance functions.
- INTEGRATO: Makes M maps of residuals & signals, and a field speed.
- FILTRA_PHASE_TEMPO: Separates non-linear deformation from atmosphere (temporal filter).

Next sections explain these steps:
- Interferometric network design.
- Phase Unwrapping
- Interferogram to phase transformation
- Linear model estimation
- Temporal filtering.

2.1. Interferometric network design

The first step is inteferometric net creation. Before this point we have master and slave images. Network is composed by interferograms. An interferogram is composed by a master and a slave image.

Some network requirements are necessary to achieve optimal results:
- Connection of all the images. This condition must be strictly satisfied.
- High redundancy of the observations. This guarantees a correct detection of the unwrapping related errors, which are also called aliasing errors.
- Uniform temporal distribution of the images. A good temporal distribution of the images provides the best configuration to describe the evolution of deformation phenomenon at hand.

Having a network that fulfils all the requirements simultaneously is practically impossible. The solution is to yield a bit on any of last three requirements after doing a previous analysis about the observations.

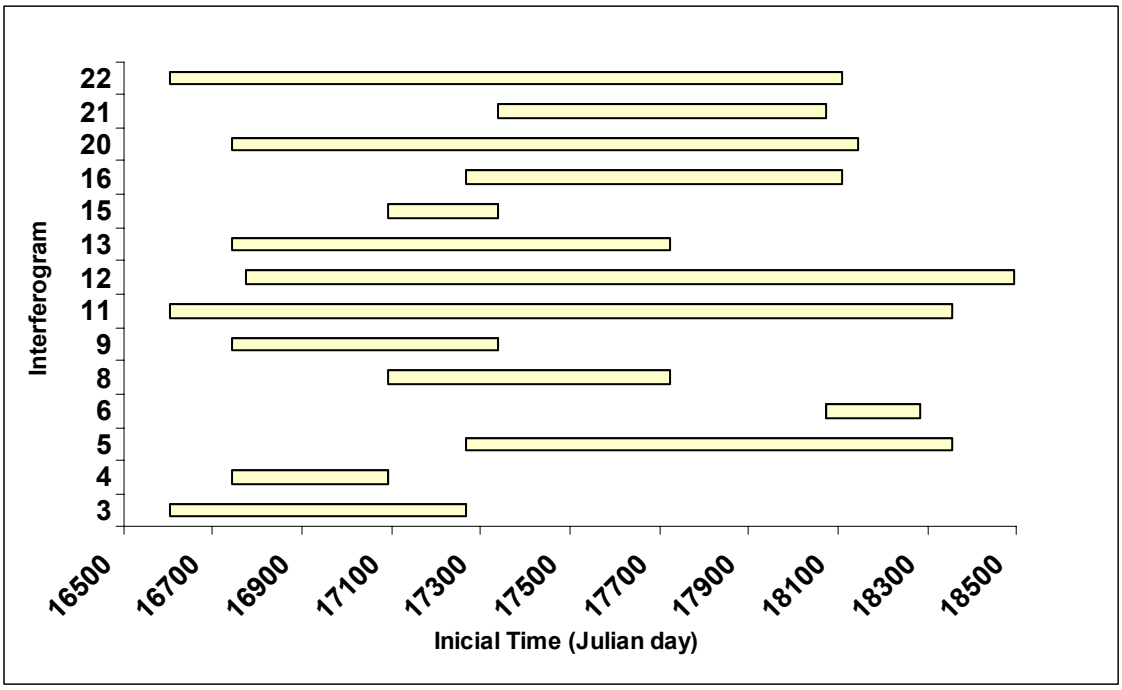

Fig. 2.2. Picture of an interferometric net.

Notes:

- This is a prove net.
- Julian day: Days from 1 January of 1950.

2.2. Phase Unwrapping

In chapter 1 are mentioned different unwrapping methods. IG uses the MCF (Minimum Cost Flow) algorithm.

In this step we have N wrapped interferograms, it is necessary unwrap them. MCF algorithm is based in the following idea:
The discrete derivates of unwrapped phases are estimated with a possible error multiple of 2Π. Difference, between discrete estimated derivates and incognita discrete derivates, is estimated. The two functions have differences multiples of 2 Π.

The interferometric wrapped phases are defined on an irregular net, cause of low coherence in some points (useless points). Then is necessary make a definition of these points using, for example, the Delaunay triangulation and then MCF algorithm is applied over this net.

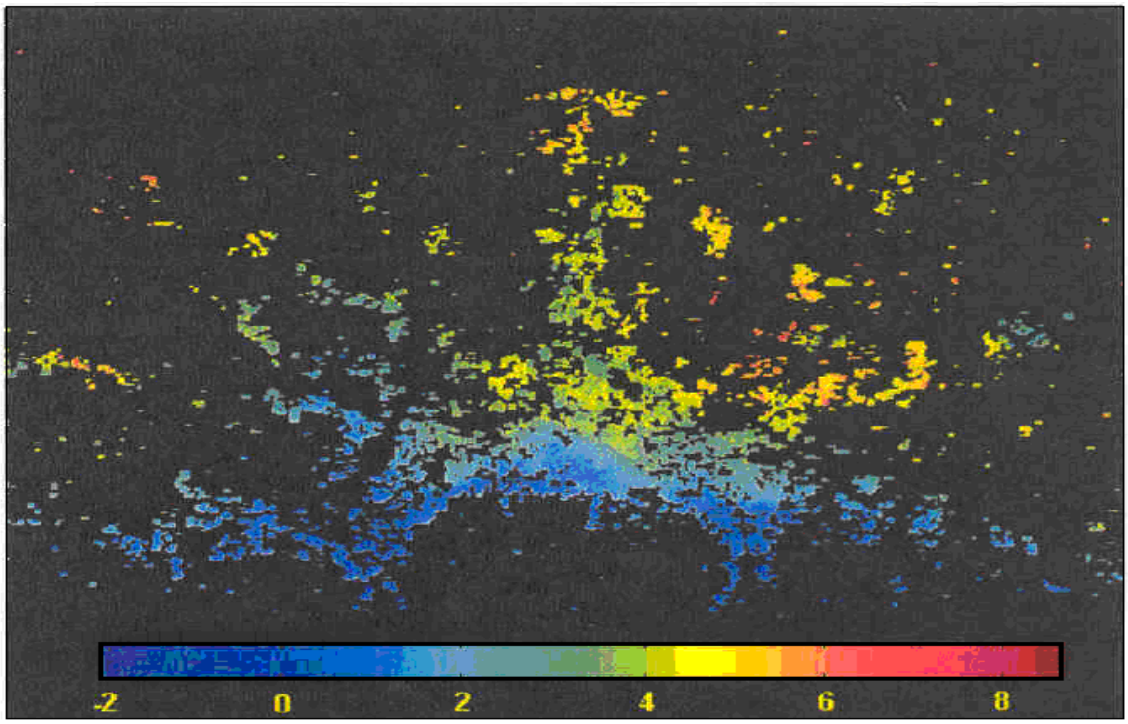

Fig. 2.3. Subsidence [cm] map (Bologna-Italia-).

From all working zone only a percentage of points are used (upper coherence pixels), see above picture. Before the unwrapping, phase had a top on ±3.14 radians (±Π); at this point phase information normally can be ±7 radians, according to the deformation and rest of parameters.

2.3. Pre-Linea

At this point we have an unwrapped interferogram network. Is necessary to mark 3 restrictions:

a) Coherence: There are a lot of points with low coherence, e.g. wood zone. The user marks a threshold coherence to delete these points. A normal value of coherence is 0.3, in the following picture is possible to see an example of pixel selection.

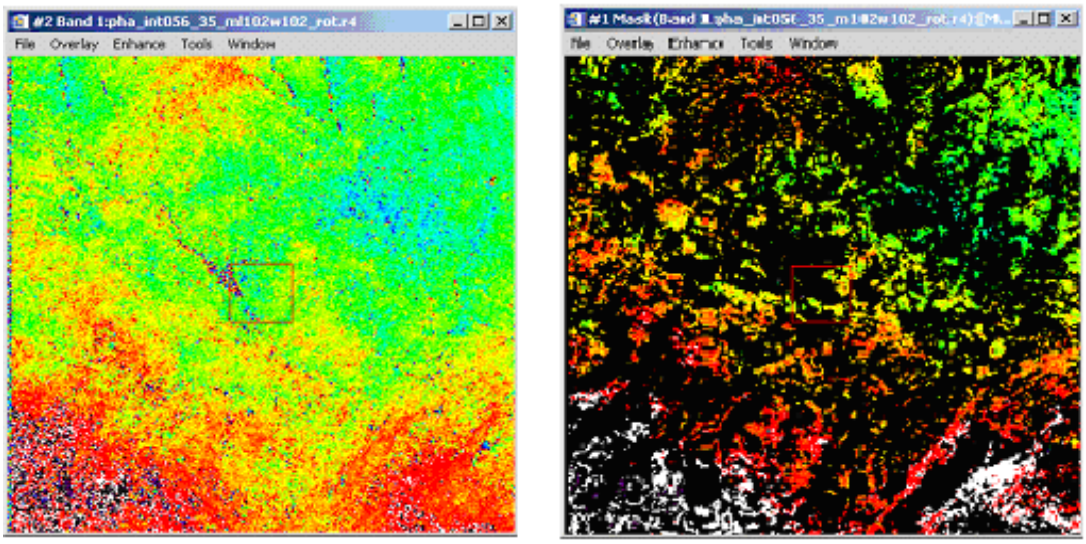

Fig. 2.4. Full phase image and filtered phase image (coherence>0.5).

Left figure shows an unwrapped phase interferogram. Each pixel has its phase value. After the threshold coherence filtering, image has a few valid pixels, right figure. If this filtering would not be executed, the final deformation estimation would be wrong.

Note: Others filtering types are possible to work, such as, *permanent scatterer,* this points selection type is based on amplitude dispersion.

b) Working zone: A SAR image covers an area of 10000 Km^2 (100 x 100 Km), due procedure complexity is impossible compute all data, is necessary make a selection of the working zone.

c) Stable area: Interferogram shows a phase difference. But is useful have a reference (null subsidence zone) for all images. Without stable area is impossible build a temporal evolution of deformation.

2.4. Interferogram to phase transformation

Now we have M images available, which cover the same area and are ordered temporally. From them we derive N, with N > M, unwrapped and co-registered interferograms, which represent the main DInSAR observations. These observations include the following components: the terrain movement contribution, Φ_{mov}; the atmospheric contribution, Φ_{atmo}; the unwrapping errors, Φ_{unwrap};, the residual topographic error, Φ_{etopo}; and the phase noise, Φ_{noise}. For each pixel of a given interferogram we can write:

$$\Delta\Phi_{int} = \Phi_{mov\_S} - \Phi_{mov\_M} + \Phi_{atmo\_S} - \Phi_{atmo\_M} + \Phi_{unwrap} + \Phi_{etopo} + \Phi_{noise} \qquad \textbf{(2.1)}$$

Where the subscripts S and M indicate the contribution of the slave and master images, respectively. Each interferogram contains the information related to the terrain movement that corresponds to the time separation between its two images. This information is not ordered temporally. In order to derive observations that are ordered with respect to the time, we need to apply the interferogram to image transformation. For each selected pixel we use this simple model:

$$\Delta\Phi_{\text{int}} = \Phi_s - \Phi_m + r_i \quad ; \quad \Phi_1 = 0 \qquad \textbf{(2.2)}$$

Where:

$\Delta\Phi_{int}$ is the interferometric phase,

$\Phi_S = \Phi_{mov\_S} + \Phi_{atmo\_S}$, is the unknown phase of the slave image,

$\Phi_M = \Phi_{mov\_M} + \Phi_{atmo\_M}$, is the unknown phase of the master image,

r_i is the residual, which should include the non-modelled part of the phase: Φ_{noise}, Φ_{unwrap}, and Φ_{etopo},

Φ_1 is the phase of the first image.

Note that this model is similar to that of an altimetric network based on geometric levelling, where the interferometric phases play the role of height differences, and the image phases are the heights, which are computed with respect to a reference point. For this reason we say that a set of N interferograms and M images represents a “network”.

The goal of this step is to estimate the phases of the M-1 images. This is achieved by a weighted LS adjustment. In order to get an appropriate estimation of the M-1 unknowns, the contribution of the non-modelled components of the observations, Φ_{noise}, Φ_{unwrap}, and Φ_{etopo}, have to go in the residuals. To this end, after the 1st LS iteration, where all the observations receive the same weight, we perform an outlier rejection based on the data snooping of Baarda by re-weighting the observations before running the 2nd LS iteration.

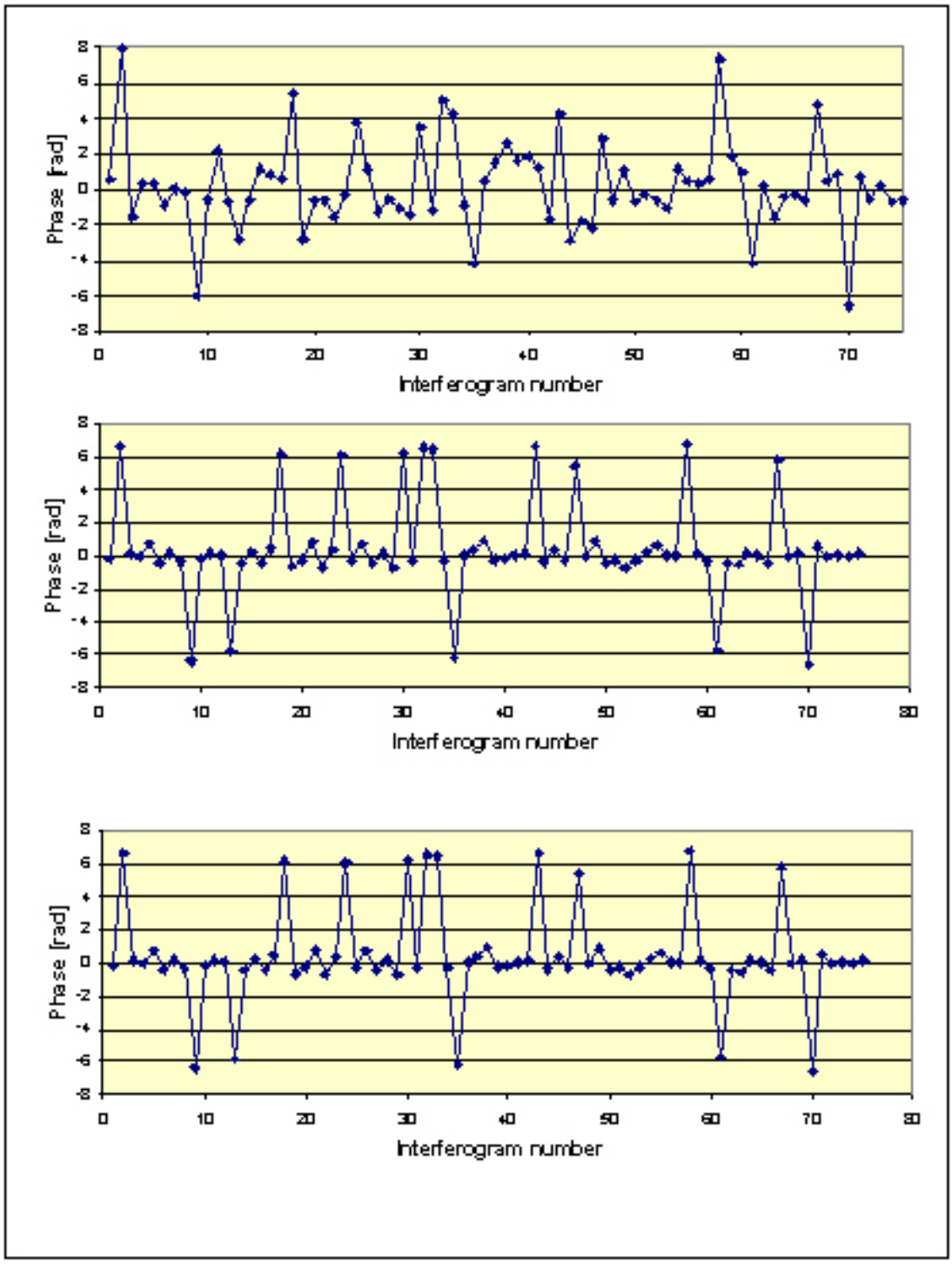

Fig. 2.5. Good outliers rejection (75 interferograms and 16 images)

In a high redundancy network there is a good outliers rejection, see fig 2.5.

- Upper picture: Profile of residuals after the 1st iteration.
- Medium picture: Profile of residuals after the 2nd iteration.
- Lower picture: Profile of simulated aliasing and noise.

Medium and lower pictures are nearly equal.

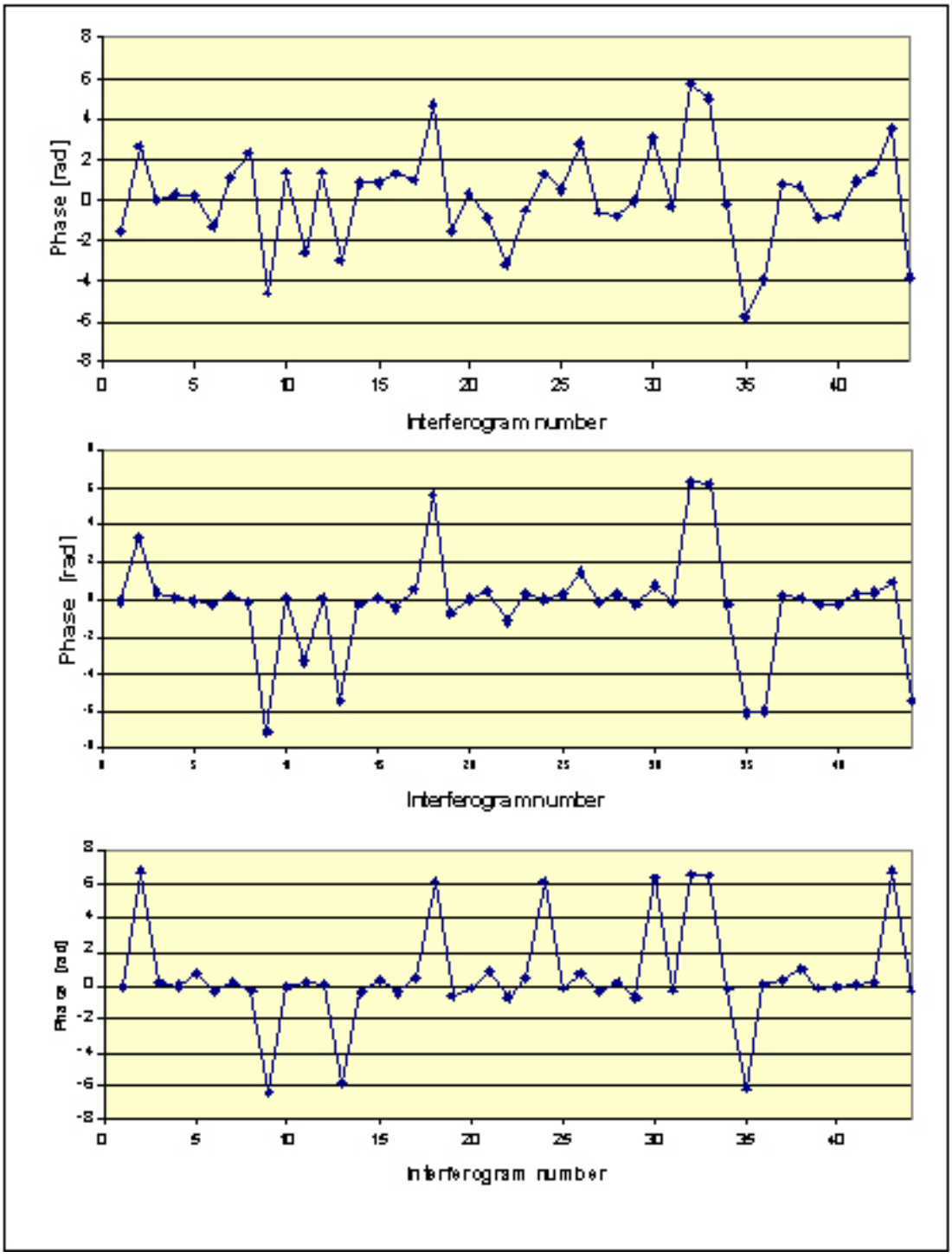

Fig. 2.6. Bad outliers rejection (44 interferograms and 16 images).

In a poor redundancy network there is a bad outliers rejection, see above figure.

- Upper picture: Profile of residuals after the 1st iteration.
- Medium picture: Profile of residuals after the 2nd iteration.
- Lower picture: Profile of simulated aliasing and noise.

Medium and lower picture are not nearly equal. There are some aliasing errors. This error charged into movement will affect final estimation.

2.5. Linear model estimation

The goal of this step is to separate the linear movement component from the atmospheric and non-linear movement component of the image phases that are estimated in the first step. To this end, we need appropriate modelling tools. This is our approach:

- We use a deterministic model for the movement component, using a stepwise linear function, i.e. dividing the observed period in intervals, where the velocity is assumed constant.
- We model stochastically the atmospheric component.
- We estimate both components by using the LS collocation technique. This is the reason why we call this step “integrated adjustment”. The aim of the integrated approach is to obtain the estimation of unknown deterministic parameters and the stochastic part, in one step.

This is the used model:

$$\Phi(t_i, l, k) = \sum_j v_j(l,k) \cdot \Delta t_j + s_{t_i}(l,k) + n_{t_i}(l,k) \qquad \textbf{(2.3)}$$

Where:

t_i is the time of acquisition of the considered image.

l, k are the image coordinates of the considered pixel.

The first term represents the deterministic model, the stepwise linear function, which includes the unknown velocities, $v_j(l,k)$, one for each interval j.

$s_{t_i}(l,k)$ is the so-called signal, i.e. the spatially correlated part of the residual of the deterministic model. The signal contains both the atmospheric component, and the non-linear part of the movement. These two components are separated in the third step of the procedure, the temporal filtering.

$n_{t_i}(l,k)$ is the noise, which is the spatially uncorrelated part of the residuals of the deterministic model.

The complete procedure includes the following steps:

1) Run LS estimation with only the deterministic model.
2) Analyse, image wise, the residuals of this adjustment, $r_{t_i}(l,k) = s_{t_i}(l,k) + n_{t_i}(l,k)$. The aim is to highlight the correlated part (signal), due to atmosphere and/or non-linear movement.

Compute of empirical autocovariance function (EAF) of the residuals.
Estimate the model autocovariance function (MAF). Note that the estimation of EAF and MAF is performed in the 2D domain.

Build the variance-covariance matrix of the residuals starting from the MCF.

3) Compute the solution, by using the LS collocation procedure, getting a set of velocities, $v_j(l,k)$, per each pixel; the signal $s_{t_i}(l,k)$ of each image t_i; and the noise $n_{t_i}(l,k)$ of each image t_i, which is used to assess the estimation quality.

A key element in the above estimation is the variance-covariance matrix. In order to assess the quality of the estimates we check the noise $n_{t_i}(l,k)$ of each image t_i. In principle, this should be spatially uncorrelated. If it is not the case, a second iteration of the LS collocation must be run. In this case the observations are given by the noise $n_{t_i}(l,k)$ of the 1st iteration.

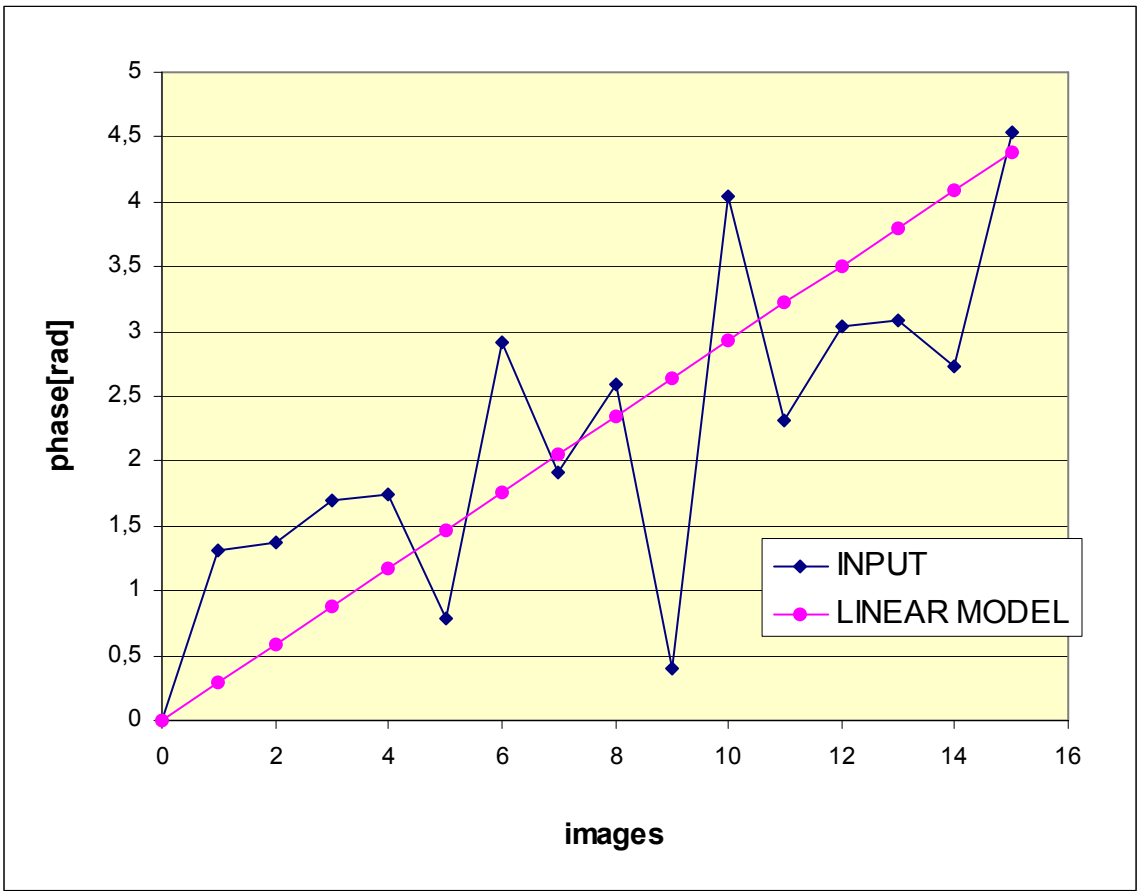

Fig. 2.7. Linear model estimation.

Picture 2.7 shows a 16 samples graphic. In blue, input of this step (pixel deformation corrupted by atmosphere). In pink, linear model created by Integrated Adjustment. The input of temporal filtering, the final step, is the difference between these 2 components.

2.6 Temporal filtering

The goal of this step is to separate the non-linear deformations from the atmospheric component, starting from the signal estimated in the previous step. For this purpose we use the following properties:

- The atmospheric component is the temporally uncorrelated part of the signal.
- The non-linear deformation shows a temporally correlated behaviour.

In order to exploit these properties we perform, pixel wise, a temporal filtering of the signal $s_{t_i}(l,k)$, which is based on the same LS collocation procedure mentioned in the previous section. The procedure includes the estimation of EAF, MAF, and of the variance-covariance matrix. In this case we work in a 1D space, i.e. for a given pixel (l,k) we have a vector of $s_{t_i}(l,k)$, one for each image.

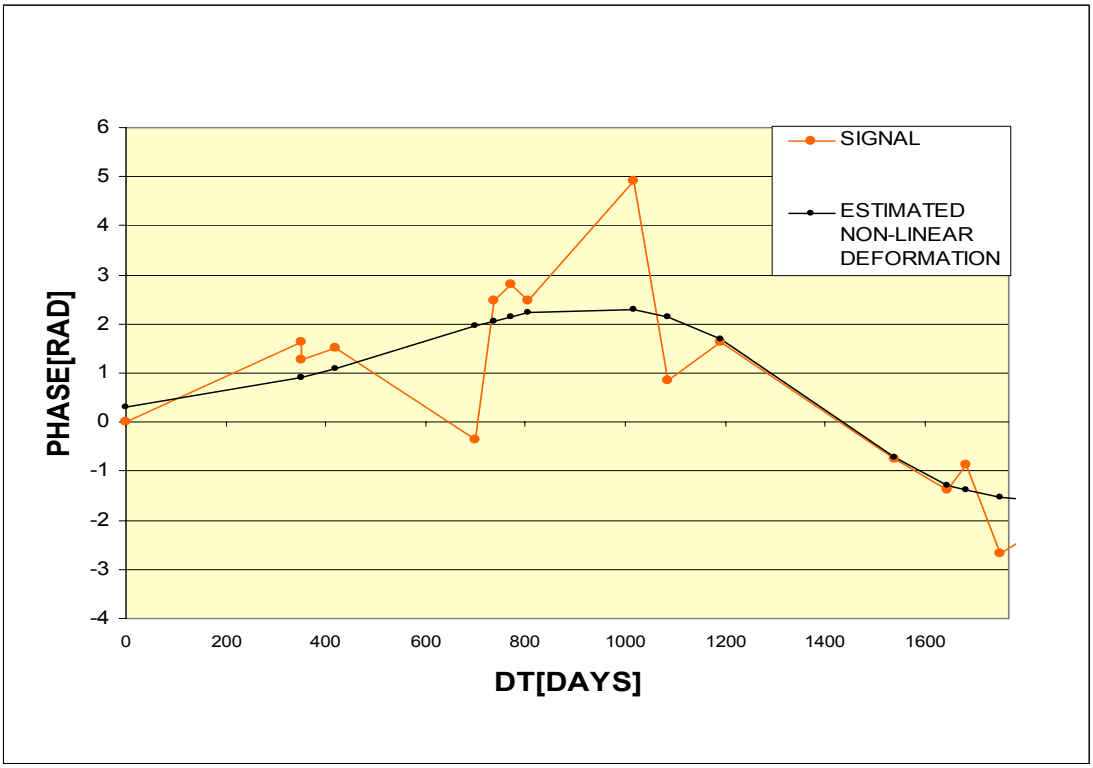

Fig.2.8. Example of temporal filtering.

This figure shows a 15 samples graphic during approximately 4,5 years. In orange, the input, in black the non-linear deformation estimation carried out by collocation method. It's clear that this methods is approximated, and others filtering give us another results.

CHAPTER 3. EXPERIMENTAL PART

In this chapter we explain the results of the procedure explained in last part over a simulated network. We created a virtual subsidence with typical errors, and applied the IG procedure to make a study of its efficiency.

3.1 Simulation description

The simulation is based in these 4 points:

- Deformation: Virtual subsidence.
- Noise and aliasing: Random values noise and a few aliasing values.
- Atmosphere: Spatial correlated values.
- Network: Type of interferogram network.

3.1.1 Deformation

The aim of this step is to have a non-linear deformation; linear deformation estimation is easier than non-linear. Deformation must have typical subsidence values. Virtual deformation is sinusoidal in time domain and an ellipse in spatial domain.

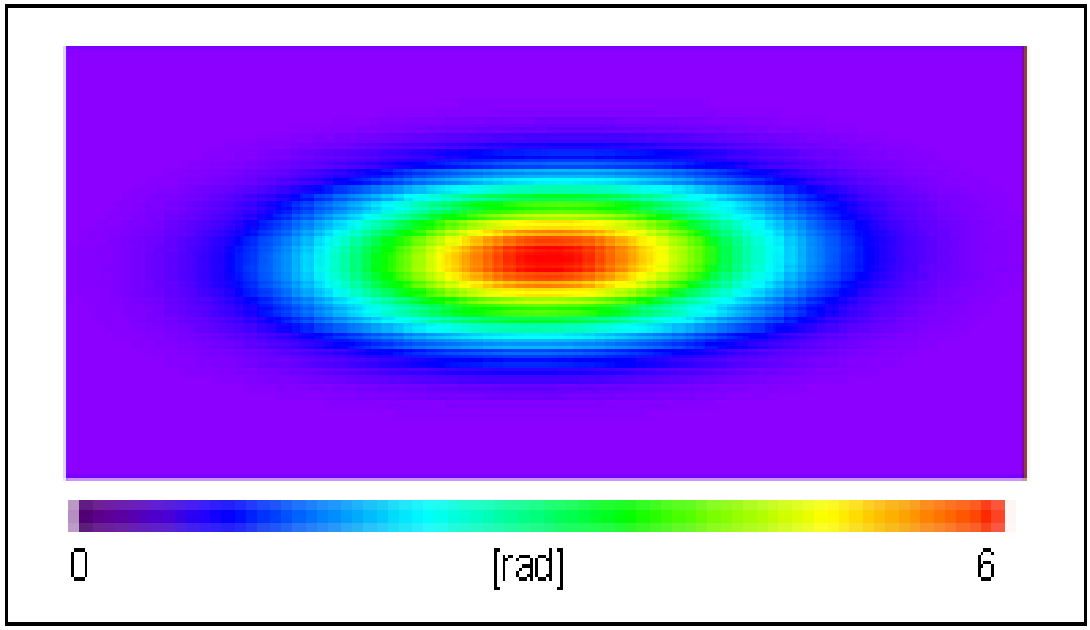

Fig. 3.1.Picture of simulation deformation (ellipse).

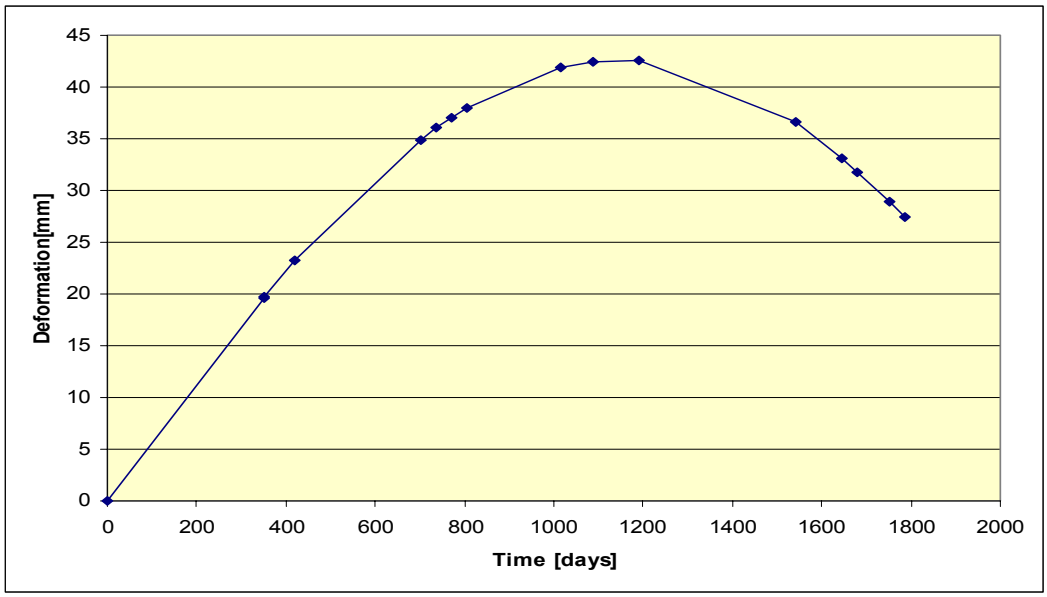

Fig. 3.2. Deformation simulation of maximum subsidence pixel.

All simulated pixels deformation have 15 samples around almost 5 years. Until 1200th day curve raises, but then it begins to diminish. It has the top on 4,3 cm of subsidence. The above picture shows the maximum subsidence pixel, it has the subsidence top on 43 millimetres.

3.1.2 Noise and Aliasing

Noise was produce randomly and with a maximum of 6 radians. Left picture shows noise amplitude. Right picture is the noise histogram.

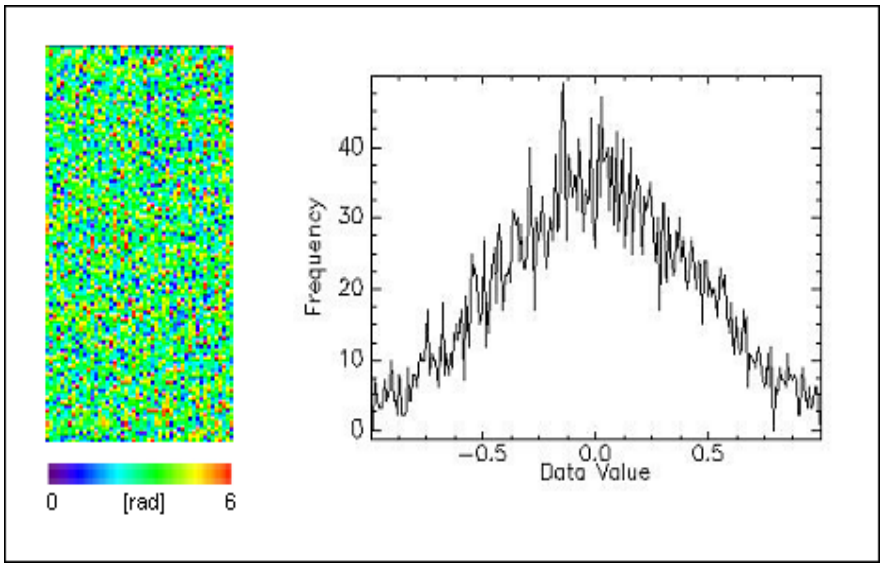

Fig. 3.3. Interferogram noise & noise histogram.

Aliasing was introduced randomly too. An aliasing error is always a 2Π multiple.

3.1.3 Atmosphere

Atmosphere was introduced randomly into interferogram net. Here there is an example of 5 atmospheres:

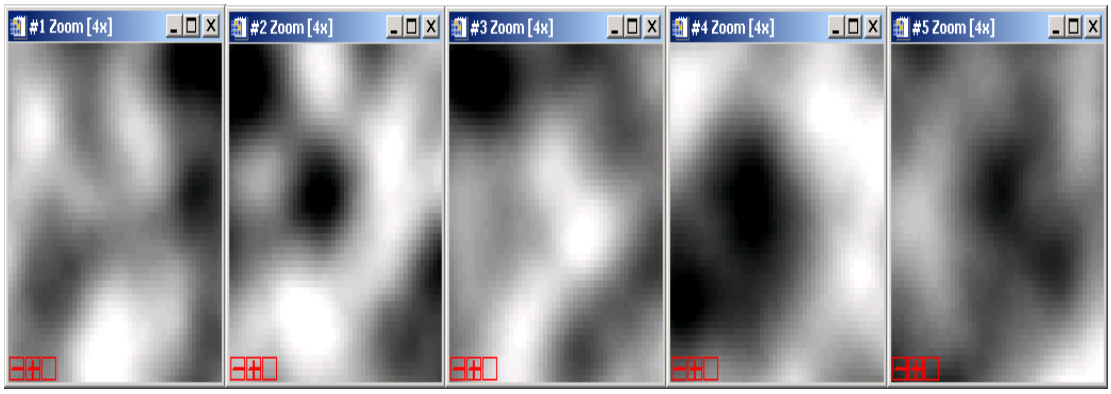

Fig. 3.4. Simulated atmosphere images.

3.1.4 Network

The network of the test consists on 16 images and 44 interferograms, good redundancy. A priori, this fine redundancy rejects the outliers and minimizes the noise.

3.2 Linear model

At this point, after outliers rejection, noise and aliasing have been minimized nearly perfectly. This is the first conclusion: noise minimization and outliers rejection work fine.

Integrated adjustment carries out 2 linear models calculation of signal, in two different iterations. Signal is estimation of deformation + atmosphere.
The aim of this step is check the fine or wrong linear estimation of deformation. Next pictures show this linear model in 3 different cases:

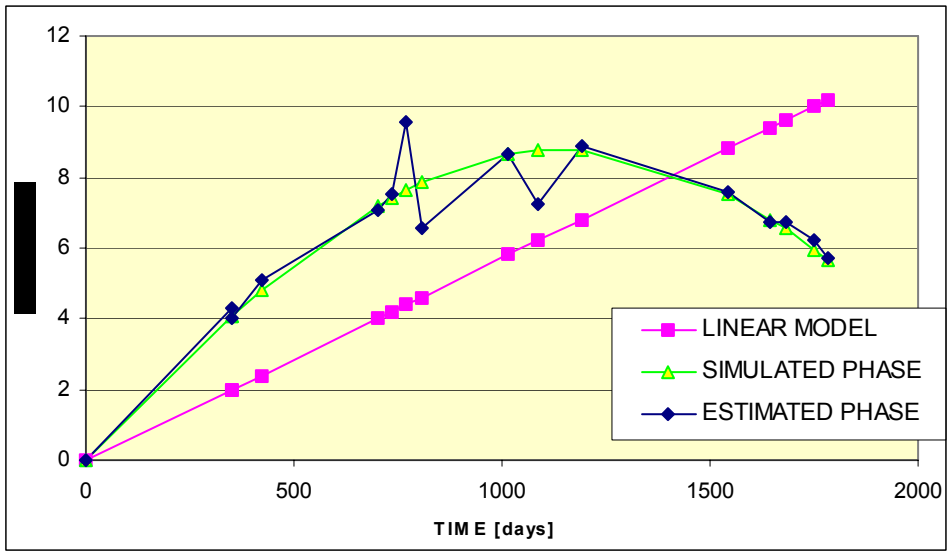

Fig. 3.5. Maximum subsidence pixel. Linear Model (Velocity = 9,39 mm/yr).

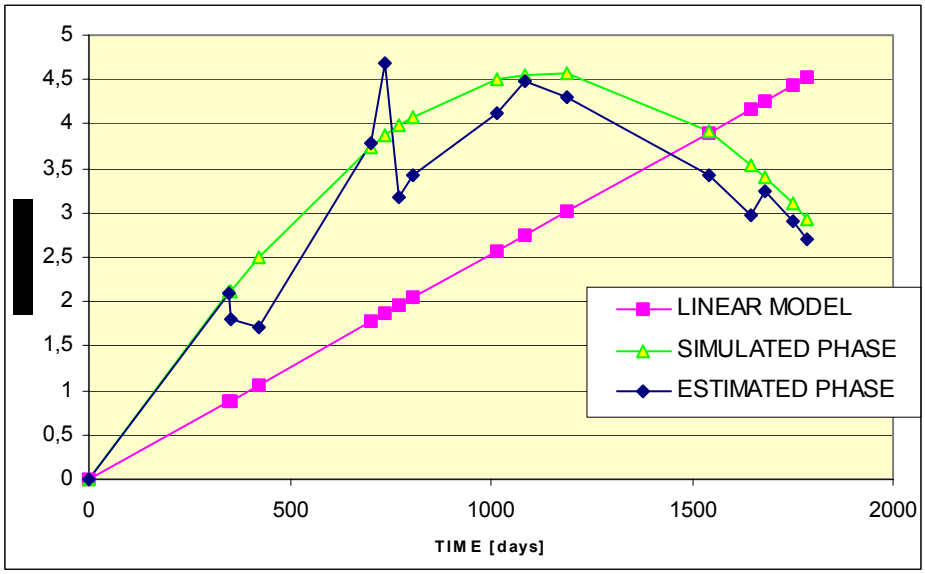

Fig. 3.6. Medium subsidence pixel. Linear Model (Velocity =4,16mm/yr)

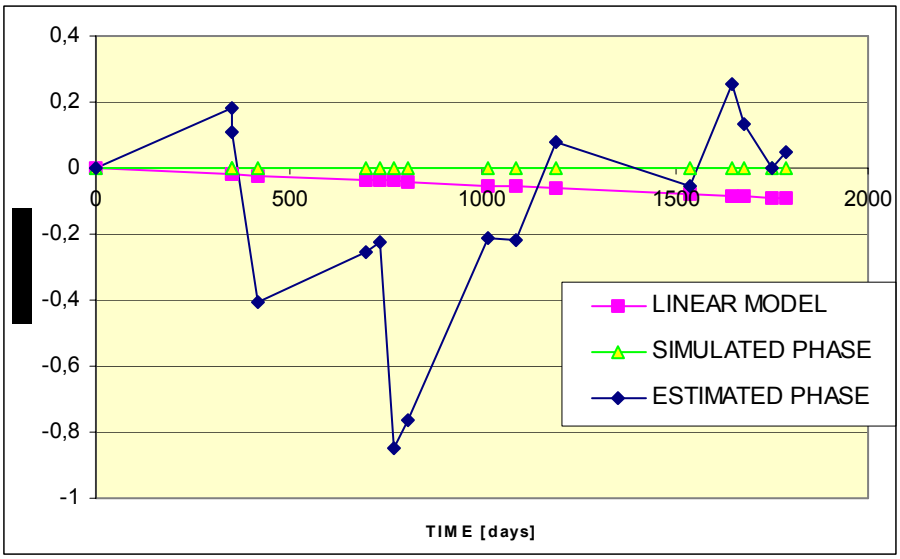

Fig. 3.7. Stable pixel. Linear Model (Velocity = -0,08mm/yr)

In blue, estimated phase is the INT2IMA deformation estimation.
In pink, linear model of integrated adjustment.
In green, simulated deformation.

Atmospheric error is more evident in stable pixel. The less subsidence pixel, the higher relative error.

3.3 Temporal filtering

Temporal filtering is a very important step of integrated adjustment. The final result depends very much on this part. One of my works was the improvement of temporal filter.

Temporal filtering input (signal) is the amount of non-linear deformation and atmosphere, and then is necessary filtering to separate these 2 different information.

The IG used filter was the media filter, which computes the media in a window (n samples) and gives this value to the centre window point. The length has to be impairing, about 5 or 7, therefore a half window of 3 or 4. It is evident that this system is not accuracy.

Now we explain some possible filters to achieve our objective:
- Median filter.
- Low Pass Band (LPB) Filter.
- Collocation Method.

MEDIAN FILTER:

First idea was median filter, is the same that media filter but it makes the median of window, and not the media. At this way if we have a window with outliers danger, this filtering can be better than media. Anyway, these 2 are inefficient filters.

LOW-PASS BAND FILTERING:

The LPB Filter was the first implementation. A LPB filter takes away noise, in our case atmosphere. This solution have a clear problem:

A typical input of temporal filtering of the IG procedure has 15 or 20, 25 as maximum. These are so few samples for a LPB filtering, because impulsional response of a LPB filter corrupts the beginning of input.

COLLOCATION METHOD:

Finally we found a good solution for this problem. Using collocation method in 1 dimension (time) we have a precise non-linear deformation estimation. The greatest quality of this method is that it can calculate itself its frequency cut, or rather, its softness for each pixel.

In next figure, there is a sinusoidal deformation summed with noise (yellow curve), collocation method make a fine approximation of corrupted input, giving, in pink, the estimated non-linear deformation.

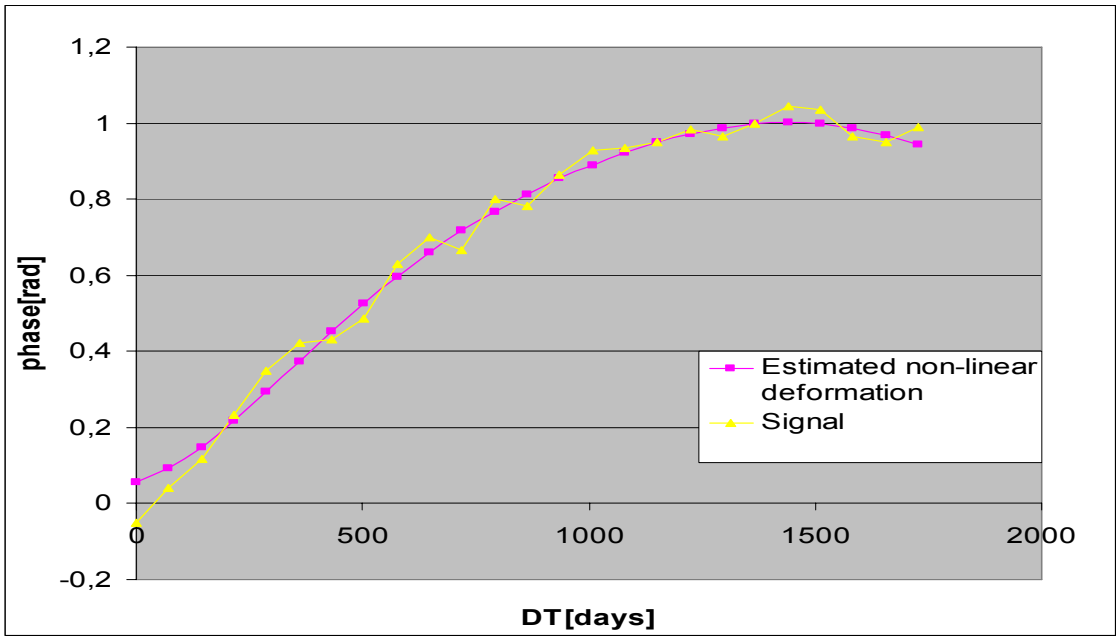

Fig. 3.10. Collocation filtering (25 samples).

3.4 Results evaluation

In 3 cases (maximum, medium and stable pixel) the final deformation estimation is fine. There is a very small error. But the most important conclusions are these:

- Interferometric noise corrupts not much the deformation estimation.
- With a high redundancy network aliasing errors are well rejected.
- Collocation methods filter well, atmosphere estimation is fine.
- Part of non-linear movement is charged into residuals. That's why in the spatial filtering some pixels are correlated in time domain.

In figure 3.11 can see a pixel deformation estimation of the IG procedure and in figure 3.12 the new estimation, in this figure we made a temporal filtering over correlated spatial residuals. This solution is more accurate.

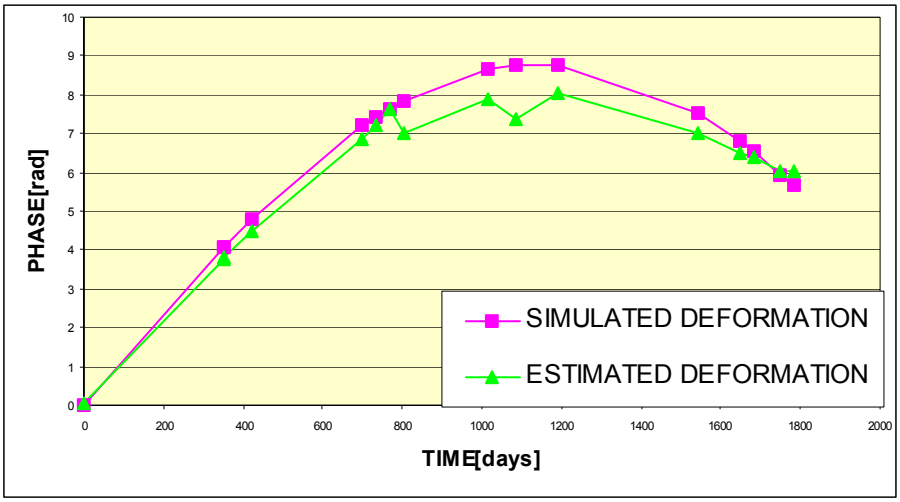

Fig. 3.11. A pixel deformation estimation.

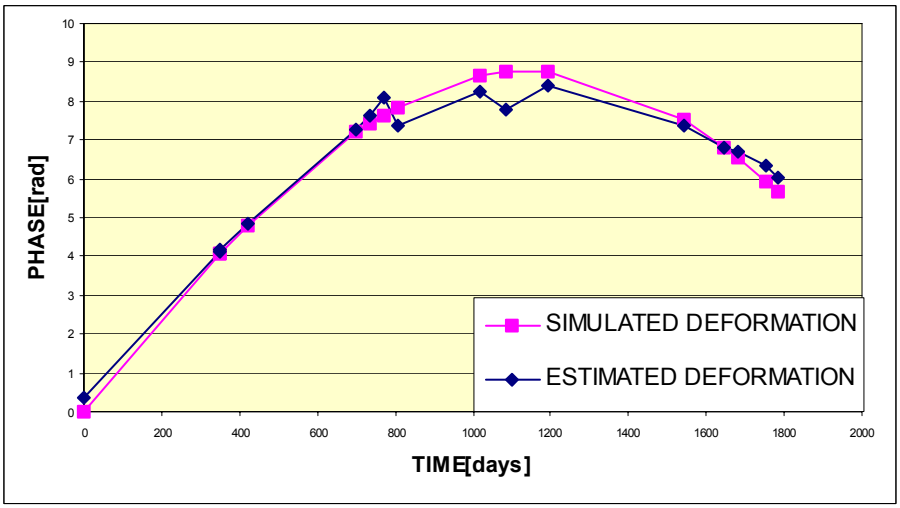

Fig. 3.12. A pixel deformation estimation (using temporal filtering over correlated spatial residuals).

CONCLUSIONS

This project describes the procedure to make deformation estimations through Differential Interferometric SAR. The document reviews the essential radar concepts, the whole IG procedure, which uses SAR images to derive deformation maps of working zone, and a study of the software quality.

After all study of Interferometry, we can comment that land deformation estimation thought Interferometry has some general limitations, like:

- Low coherence in wood zones: Actually non-urban zone are difficult to study. These areas have low coherence with a small temporal base. This restriction is also present in determined time periods in urban zones when buildings are changing.
- Calculation precision depends on sampling temporal frequency of satellites.
- Atmosphere produce strong effects, which are not possible to erased before to begin the procedure.

During the experimental part of this project, it was proved that the estimation of deformation works successfully. The procedure obtains very fine results, with only small errors. This procedure is continuously improving, although it represents already an accurate tool for deformation monitoring.

During my stay at Institute of Geomatics, I have been part of “Teledetecció Activa” (TA) Unit, where interferometry applications are studied. The people of TA carry out some tasks as creating deformation maps, making new software or improving software for earth monitoring (topography and deformation estimation), etc. In these months I collaborated to prepare some reports and one of articles that the Institute will present in the 6th Geomatic Week, a Conference devoted to geomatics, which will be held in Barcelona in February 2005. This paper is attached in the annex of this work.

BIBLIOGRAPHY

- Curlander, J. C. and Mcdonough, R. N., "*Synthetic Aperture Radar: Systems and Signal Processing*", Wiley-Interscience, (1991).

- Lillesand, T. M. and Kiefer, R. W., "Microwave Sensing", Cap. 8 in *Remote Sensing and Image Interpretation*, pp. 616-710, John Wiley & Sons, Inc., (2000).

- Ramon F. Hanssen, "*Radar Interferometry: Data Interpretation and Error Analysis*", Kluwer Academic Publishers, (2001).

- Small, D., "*Generation of Digital Elevation Models through Spaceborne SAR Interferometry*", Remote Sensing Series, vol. 30, (1998).

- Usai, S., "*A New Approach for Long-term Monitoring of Deformations by Differential SAR Interferometry*", doctoral tesis of The Delft Technical University, (2001).

- http://earth.esa.int

- http://www.asf.alaska.edu/apd/software/insar/interferogram.html

- http://www.gmat.unsw.edu.au/snap/publications/chang_etal2004d.pdf

- http://cosmech.tripod.com/Estadistica/Regres1.htm

ANNEX

TITLE: Interferometric SAR data analysis and processing

DEGRE: Technical Telecommunication Engineering
Speciality: Telecommunication Systems

AUTHOR: Álvaro Fernández Salas

DIRECTOR: Michele Crosetto

SUPERVISOR: Jaume Piera Fernández

DATE: 20th January of 2005

ADVANCED MODELLING TOOLS IN SAR INTERFEROMETRY

Monserrat O.[(1)], Crippa B.[(2)], Biescas E.[(1)], Fernandez A.[(1)], Crosetto M.[(1)]
[(1)] *Instituto de Geomática, Av. Canal Olímpic s/n, 08860 Castelldefels, España, oriol.monserrat@ideg.es*
[(2)] Dip. di Scienze della Tierra, Università di Milano, Via Cicognara 7, Milán, Italia, bruno.crippa@unimi.it

***Key words*:** Land deformation, modelling, least squares, collocation, simulated data.

Abstract

SAR interferometry represents a powerful tool for land deformation detection and monitoring. The paper focus on a chain of tools used to estimate the land deformation starting from a time series of complex SAR (Synthetic Aperture Radar) images acquired over the same area. The main goal of the chain is to estimate the linear and non-linear components of the deformation, by minimizing the effects of error sources, like the atmospheric effects, the topographic component, the unwrapping related errors, and the phase noise. In this paper a general description of the procedure is provided, focusing on three main steps: the interferogram to image transformation; the integrated adjustment, which is based on the least squares collocation technique; and the temporal filtering. The procedure is illustrated by examples based on simulated SAR interferometric data.

1. Introduction

The differential interferometric SAR technique (DInSAR), based on spaceborne SAR data, has been successfully employed in different application fields [1], like glacier dynamics [2,3]; earthquakes [4,5]; volcanoes [6,7]; landslides [8,9]; and the deformations related to water exploitation, mining activity, and construction works [10,11,12]. The above applications require different quality levels to the estimates provided by DInSAR. A rather qualitative use of the DInSAR results seems to be sufficient for the purposes of some applications. An example is given by those studies characterized by large deformations (from decimetres to meters), where even the qualitative information derived from a single interferogram, which represents the poorest DInSAR configuration, may provide a valuable data source for the geophysical interpretation. However, this is not the case for some other important applications, e.g. the deformation monitoring of important infrastructures, which needs to be characterised by high quality standards like those usually achieved by the traditional geodetic techniques. These applications need a fully quantitative DInSAR monitoring, which can be only achieved by using multiple observations of the same deformation phenomenon, i.e. by using multiple SAR images acquired over the same area, and by employing suitable data modelling and analysis procedures. It is important to note that the use of multiple DInSAR observations requires 3D modelling and data analysis tools (2D in space, plus the time).

This paper describes a new DInSAR procedure, which makes use of advanced modelling strategies to fully take advantage of the specific properties of the DInSAR observations. The proposed procedure is based on data modelling and analysis tools, like the least squares (LS) collocation, which are widely employed in geodesy. The paper provides a general description of the procedure, and illustrates its main steps through examples based on simulated DInSAR data. It is assumed that the reader knows the fundamentals of DInSAR for land deformation measurement. In particular, are supposed to be known the basic properties of the DInSAR observations, i.e. the DInSAR phases, and their main components, such as the component due to terrain topography, the terrain movement contribution, the atmospheric contribution, the errors generated in the phase unwrapping and the phase noise. A comprehensive introduction to DInSAR is given by [1]. In the same proceeding of this paper one may find a paper which describes the basics of the DInSAR technique [13].

2. Description of the proposed procedure

The DInSAR procedure implemented by the authors requires the following main input data;

- N unwrapped interferograms, derived from a set of M complex SAR images acquired over the area of interest. Note that the images must be suitable to form interferometric pairs, i.e. their spatial separation has to be typically of the order of few hundred meters.

- N coherence images, one for each interferogram. The coherence is a good indicator of the quality of the DInSAR phase: only the pixels characterized by good coherence (above a given threshold) are considered in the processing.
- Auxiliary data, which describe the main characteristics of the interferograms: master image (M), slave image (S), time separation between the two images (ΔT), perpendicular baseline ($B_\perp$), etc.
- Auxiliary data, which describe the SAR images: image dimensions, acquisition date, etc.

The outputs of the procedure include:
- The temporal evolution of the deformation for each selected pixel. The deformation is estimated in correspondence to each acquisition date of the SAR images. The date of the oldest image is chosen as temporal reference, i.e. the estimated values are relative deformation with respect to this date. The estimated deformation includes both the linear and non linear components of the deformation.
- The atmospheric contribution for each SAR image.
- The residuals of the different estimations, used to assess the quality of each step of the procedure.

Although the complete procedure may include several steps, in this paper the description is limited to the following main steps:
- The interferogram to image transformation.
- The integrated adjustment, based on the LS collocation technique.
- The temporal filtering.

2.1 Interferogram to image transformation

Let us assume that we have M images available, which cover the same area and are ordered temporally. From them we derive N, with N > M, unwrapped and co-registered interferograms, which represent the main DInSAR observations. These observations include the following components: the terrain movement contribution, Φ_{mov}; the atmospheric contribution, Φ_{atmo}; the unwrapping errors, Φ_{unwrap};, the residual topographic error, Φ_{etopo}; and the phase noise, Φ_{noise}. For each pixel of a given interferogram we can write:

$$\Delta\Phi_{int} = \Phi_{mov\_S} - \Phi_{mov\_M} + \Phi_{atmo\_S} - \Phi_{atmo\_M} + \Phi_{unwrap} + \Phi_{etopo} + \Phi_{noise}$$

where the subscripts S and M indicate the contribution of the slave and master images, respectively. Each interferogram contains the information related to the terrain movement that correspond to the time separation between its two images. This information is not ordered temporally. In order to derive observations that are ordered with respect to the time, we need to apply the interferogram to image transformation. For each selected pixel we use this simple model:

$$\Delta\Phi_{\text{int}} = \Phi_s - \Phi_m + r_i$$
$$\Phi_1 = 0$$

where:
- $\Delta\Phi_{int}$ is the interferometric phase,
- $\Phi_S = \Phi_{mov\_S} + \Phi_{atmo\_S}$, is the unknown phase of the slave image,
- $\Phi_M = \Phi_{mov\_M} + \Phi_{atmo\_M}$, is the unknown phase of the master image,
- r_i is the residual, which should include the non-modelled part of the phase: Φ_{noise}, Φ_{unwrap}, and Φ_{etopo},
- Φ_1 is the phase of the first image.

Note that this model is similar to that of an altimetric network based on geometric levelling, where the interferometric phases plays the role of height differences, and the image phases are the heights, which are computed with respect to a reference point. For this reason we say that a set of N interferograms and M images represents a "network". The goal of this step is to estimate the phases of the M-1 images. This is achieved by a weighted LS adjustment. In order to get an appropriate estimation of the M-1 unknowns, the contribution of the non-modelled components of the observations, $\Box_{noise}$, $\Box_{unwrap}$, and $\Box_{etopo}$, have to go in the residuals. To this end, after the 1st LS iteration, where all the observations receive the same weight, we perform an outlier rejection based on the data snooping of Baarda [14] by re-weighting the observations before running the 2nd LS iteration. The effectiveness of the procedure is illustrate in Figure 1, by using DInSAR simulated data. An example where the rejection does not work well is illustrated in Figure 2. The simulated data used in this work are described in Figure 3.

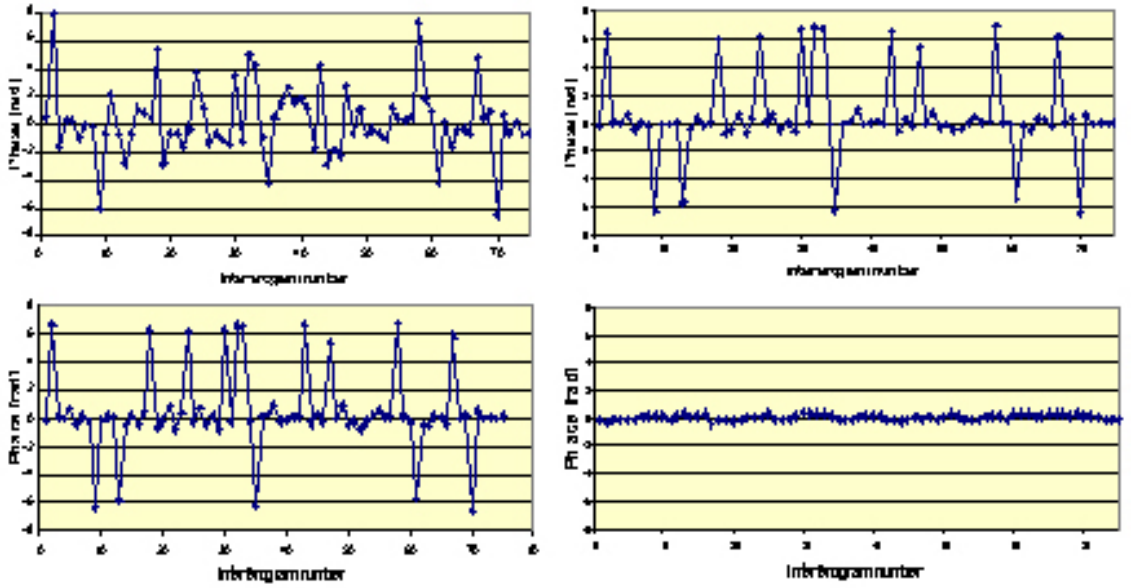

Figure 1. Example of outlier rejection over a network with high redundancy. The network consists of 16 images and 75 interferograms. All data have been simulated. Upper left: profile of residuals after the 1st iteration. Upper right: profile of residuals after the 2nd iteration. Lower left: profile of simulated noise and unwrapping error. Lower right: difference between the residuals after the 2nd iteration and the simulated: one may see that the outlier rejection works properly.

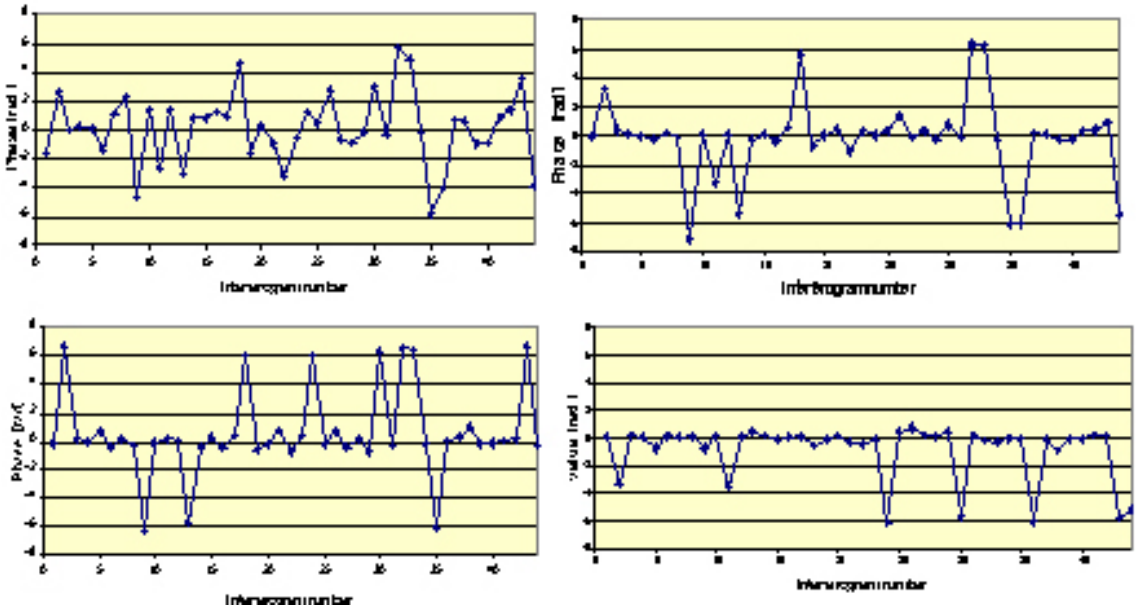

Figure 2. Example of outlier rejection over a network with lower redundancy, if compared to the Figure 1. The network consists of 16 images and 44 interferograms. All data have been simulated. Upper left: profile of residuals after the 1st iteration. Upper right: profile of residuals after the 2nd iteration. Lower left: profile of simulated noise and unwrapping error. Lower right: difference between the residuals after the 2nd iteration and the simulated noise and unwrapping error. One may see that in this case the outlier rejection does not work well for all the interferograms: in this case some of the unwrapping errors affect the estimates of the phases. This is due to the lower redundancy

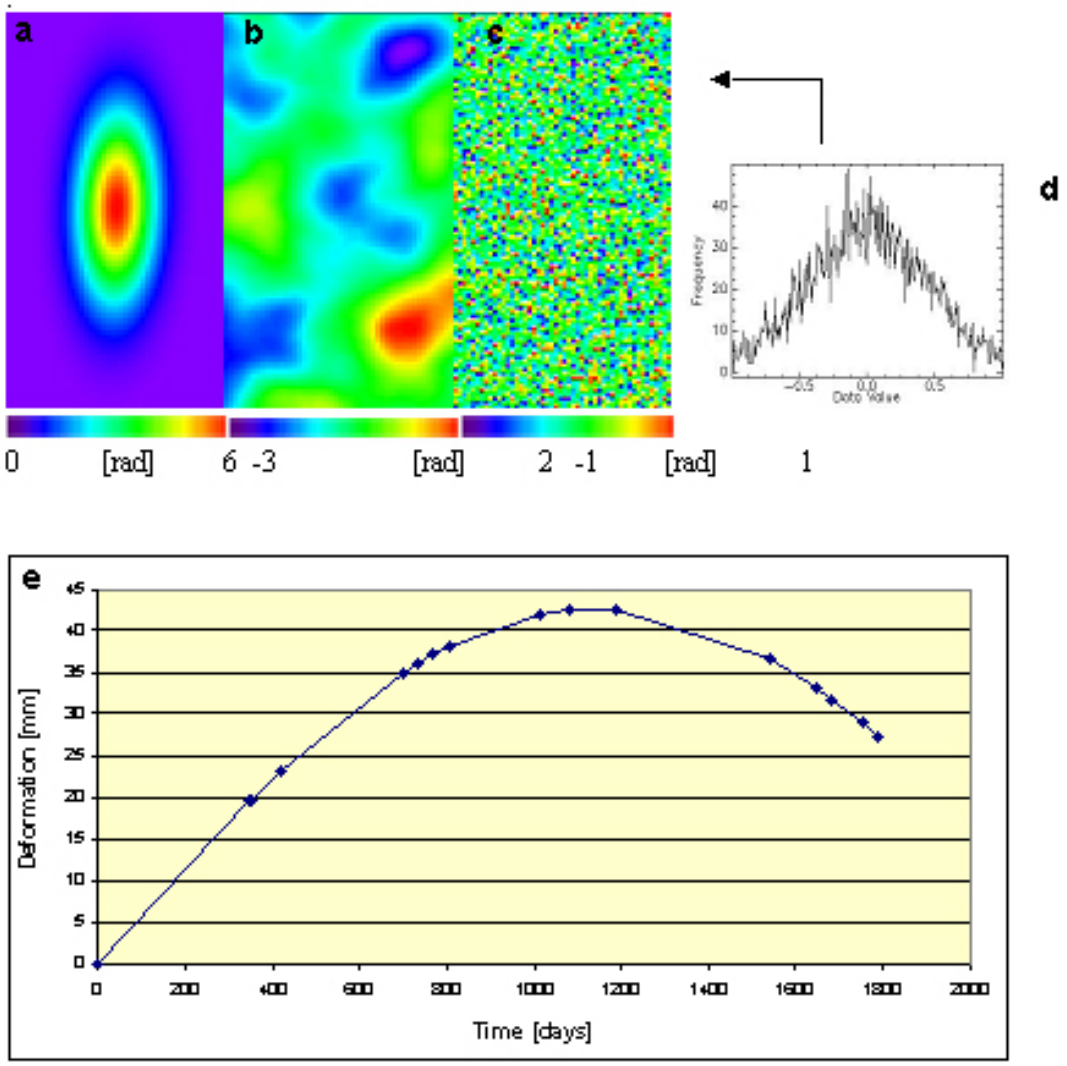

Figure 3: Description of the simulated data. The dimension of all images is 50 by 100 pixels. (a): simulated interferogram with ΔT = 710 days, where the phase only includes the movement contribution, Φ_{mov_S} - Φ_{mov_M}. (b): example of simulated atmospheric contribution, Φ_{atmo}. (c): example of simulated phase noise, Φ_{noise}, whose histogram is shown in (d). In this case the noise has zero mean and a standard deviation of 0.42 rad. (e) Profile with the temporal evolution of the simulated movement. This profile corresponds to the point with maximum deformation, located in the centre of the ellipsoid shown in (a).

The effectiveness of the outlier rejection critically depends on the type of available network, i.e. on the configuration made by the N interferograms and the M images. For this reason, the network has to be properly designed before starting the DInSAR process. This is a critical point because it plays a key role to achieve good results with the DInSAR technique. These are some of the most important requirements that are taken into account when designing a DInSAR network:

1. Connection of all the images. This condition must be strictly satisfied.
2. High redundancy of the observations. This guarantees a correct detection of the unwrapping related errors, which are also called aliasing.
3. Uniform temporal distribution of the images. A good temporal distribution of the images provides the best configuration to describe the evolution of deformation phenomenon at hand.

The importance of the network design, and in particular the relation between the redundancy and the outlier rejection is illustrated in Figures 1 and 2.

2.2 Integrated adjustment

The goal of this step is to separate the movement component from the atmospheric component of the image phases that are estimated in the first step. To this end, we need appropriate modelling tools. This is our approach:

- We use a deterministic model for the movement component, using a stepwise linear function, i.e. dividing the observed period in intervals, where the velocity is assumed constant,
- We model stochastically the atmospheric component,
- We estimate both components by using the LS collocation technique [15, 16]. This is the reason why we call this step "integrated adjustment". The aim of the integrated approach is to obtain the estimation of unknown deterministic parameters and the stochastic part, in one step.

This is the used model:

$$\Phi(t_i, l, k) = \sum_j v_j(l,k) \cdot \Delta t_j + s_{t_i}(l,k) + n_{t_i}(l,k)$$

where:

- t_i is the time of acquisition of the considered image,
- l, k are the image coordinates of the considered pixel,
- the first term represents the deterministic model, the stepwise linear function, which includes the unknown velocities, $v_j(l,k)$, one for each interval j.
- $s_{t_i}(l,k)$ is the so-called signal, i.e. the spatially correlated part of the residual of the deterministic model. The signal contains both the atmospheric component, and the non-linear part of the movement. These two component are separated in the third step of the procedure, the temporal filtering.
- $n_{t_i}(l,k)$ is the noise, which is the spatially uncorrelated part of the residuals of the deterministic model.

The complete procedure includes the following steps:

1) Run a LS estimation with only the deterministic model, see the example shown in Figures 4a and 4b.
2) Analyse, image wise, the residuals of this adjustment, $r_{t_i}(l,k) = s_{t_i}(l,k) + n_{t_i}(l,k)$. Two examples of residuals are illustrated in Figures 4c and 4d. The aims is to highlight the correlated part (signal), due to atmosphere and/or non-linear movement.

Compute of empirical autocovariance function (EAF) of the residuals.
Estimate the model autocovariance function (MAF), see an example in Figure 4e. Note that the estimation of EAF and MAF is performed in the 2D domain.
Build the variance-covariance matrix of the residuals starting from the MCF.

3) Compute the solution, by using the LS collocation procedure, getting a set of velocities, $v_j(l,k)$, per each pixel; the signal $s_{t_i}(l,k)$ of each image t_i; and the noise $n_{t_i}(l,k)$ of each image t_i, which is used to assess the estimation quality.

Let us consider the above model, writing it in terms of vectors and matrices:

$$\Phi = Ax + s + n$$

with:

$$D(\Phi) = C_{ss} + C_{nn} + C_{\hat{\Phi}\hat{\Phi}} = C_{ee}$$

where:
- Φ is the vector of the observations,
- A is the design matrix,
- x is the vector of the unknown deformation velocities,
- s is the signal due to atmosphere and/or non-linear deformation,

- n is the noise,
- D is the variance-covariance matrix of the observations.

The solution is found by solving in two separated stages the following two systems:

$$\Phi = Ax + e$$

$$e = s + n$$

This is the LS solution:

$$\hat{x} = \left(A^t C_{ee}^{-1} A\right)^{-1} A^t C_{ee}^{-1} \Phi$$

$$\hat{e} = \Phi - A \cdot \left(A^t C_{ee}^{-1} A\right)^{-1} A^t C_{ee}^{-1} \Phi = \left[I - A \cdot \left(A^t C_{ee}^{-1} A\right)^{-1} A^t C_{ee}^{-1} \right] \Phi \equiv H\Phi$$

$$\hat{s} = C_{ss} C_{ee}^{-1} \hat{e} = C_{ss} C_{ee}^{-1} \left(\Phi - A\hat{x}\right)$$

$$\hat{n} = C_{nn} C_{ee}^{-1} \left(\Phi - A\hat{x}\right)$$

Finally, by applying the law of covariance propagation, we can find the variance-covariance matrices of the estimates.

A key element in the above estimation is the variance-covariance matrix. In order to assess the quality of the estimates we check the noise $n_{t_i}(l,k)$ of each image t_i. In principle, this should be spatially uncorrelated. If it is not the case, e.g. see Figure 5, a second iteration of the LS collocation have to be run. In this case the observations are given by the noise $n_{t_i}(l,k)$ of the 1st iteration.

2.3 Temporal filtering

The goal of this step is to separate the non-linear deformations from the atmospheric component, starting from the signal estimated in the previous step. For this purpose we use the following properties:

The atmospheric component is the temporally uncorrelated part of the signal,
The non-linear deformation shows a temporally correlated behaviour.

In order to exploit these properties we perform, pixel wise, a temporal filtering of the signal $s_{t_i}(l,k)$, which is based on the same LS collocation procedure mentioned in the previous section. The procedure include the estimation of EAF, MAF, and of the variance-covariance matrix. In this case we work in a 1D space, i.e. for a given pixel (l,k) we have a vector of $s_{t_i}(l,k)$, one for each image. An example of temporal filtering over the signal $s_{t_i}(l,k)$ of 25 images is shown in Figure 6. One may compare the temporally correlated part of the signal, i.e. the estimated non-linear component of the movement, and the simulated non-linear deformation. The EAF of the input signal is shown Figure 7.

Acknowledgements

A part of this work has been funded by the Spanish Ministerio de Educación y Ciencia, through the project of the National Programme of Natural Resources named AURORAE (*Aplicaciones de la teledetección para la gestión de recursos naturales*), under the contract number REN2003-00742, and through the Integrated Action between the Institute of Geomatics and the University of Milan, with reference HI2002-0029.

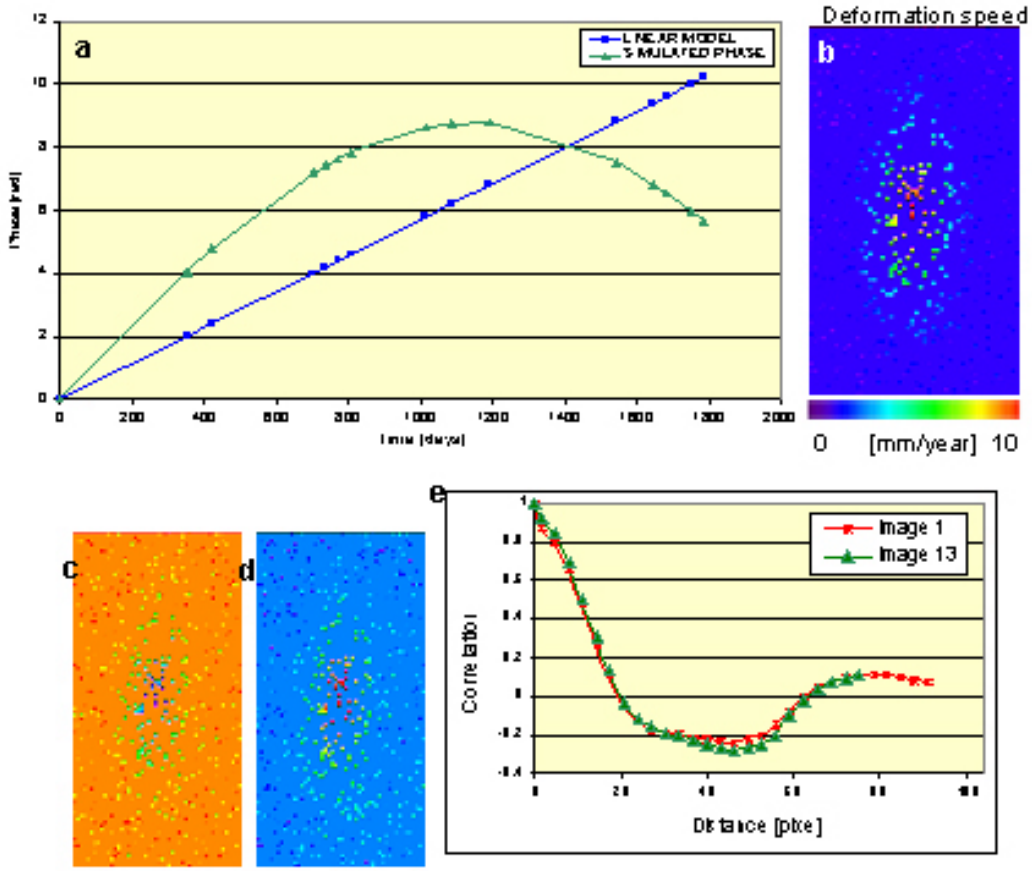

Figure 4. Integrated adjustment. (a, b): results of the LS estimation with only the deterministic model, using one interval for the entire observed period. (a) Temporal profile of a pixel, where are shown the estimated linear model and the simulated image phases. (b) Field of the estimated deformation speed. (c), image 1, and (d), image 13: two example of the residuals of the LS adjustment. In (c) the residuals are distributed in the range [-2.5; 0.6 rad], while in (d) the range is [-0.3; 2.7 rad]. One may notice that the residual are spatially correlated, with a pattern that is similar to that of the deformation speed (b). The spatial correlation of the residuals can be due to the atmospheric component, and the non-linear deformation. In this case the correlation is due to the non-linear evolution of the deformation. (e) Two EAFs of the residuals shown in (c,d). As already mentioned, the two fields are highly spatially correlated.

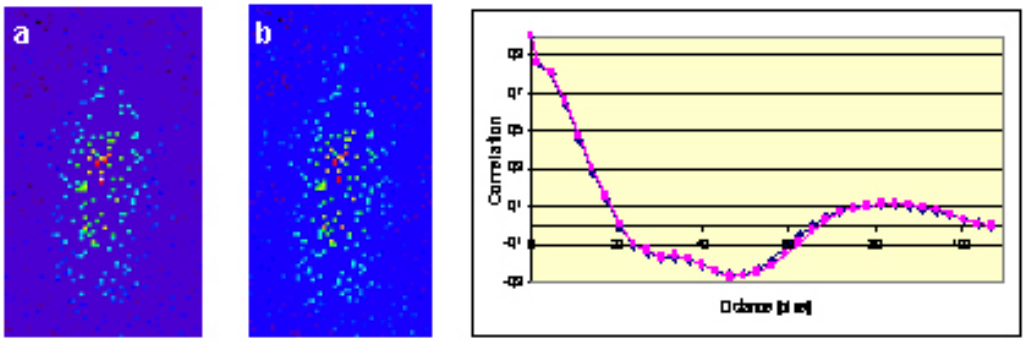

Figure 5. Integrated adjustment. (a, b): Example of two residuals after the LS collocation. Both residuals show a high spatial correlation, see their EAFs. The magnitude of these residuals is smaller than that of those shown in Figure 4c and 4d. In (a) the residuals are distributed in the range [-0.1; 0.6 rad], while in (b) their range is [-0.1; 0.4 rad]. In this case it is necessary to run a 2nd iteration of the LS collocation.

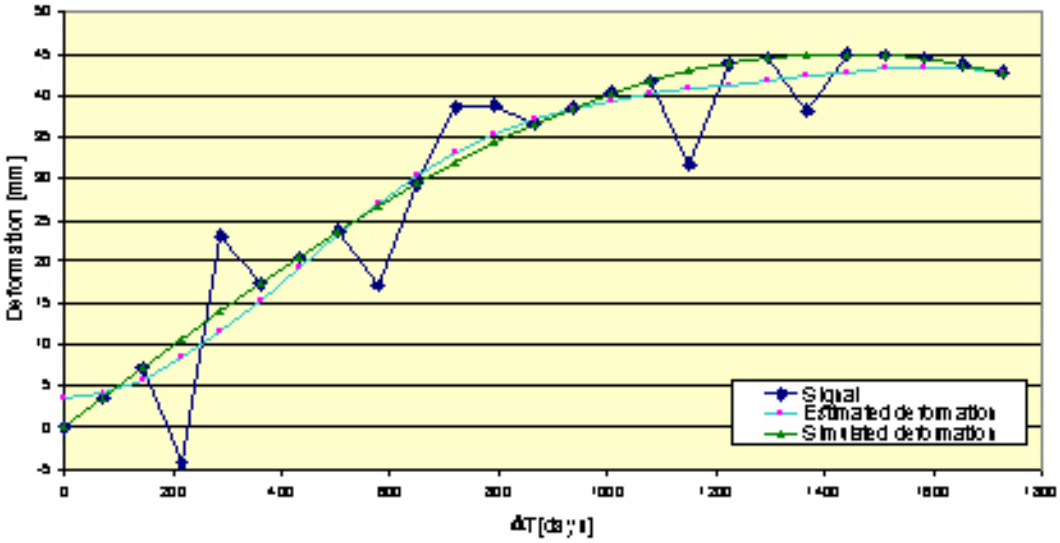

Figure 6: Example of temporal filtering over a signal $s_{t_i}(l,k)$ of 25 images. The profile includes three types of data: the input signal (Signal); the temporally correlated part of the signal, which represents the non-linear component of the movement (Estimated deformation); the simulated non-linear deformation (Simulated deformation), which can be used to check the quality of the estimated deformation.

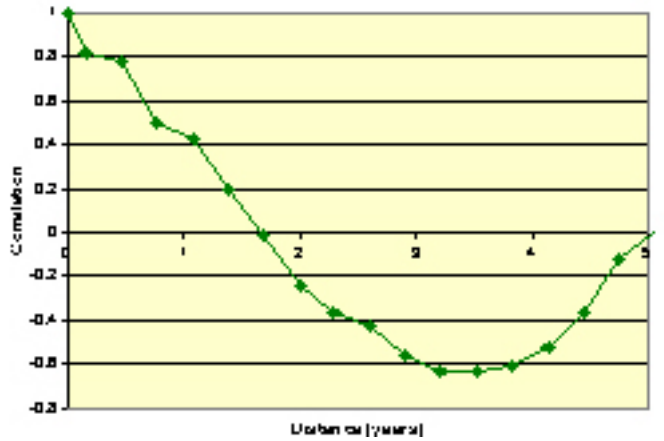

Figure 7: EAF of the input signal shown in Figure 6.

References

[1]. Hanssen, R., 2001. Radar interferometry. Kluwer Academic Publishers, Dordrecht, Holland, p. 308.
[2]. Goldstein, R.M., Englehardt, H., Kamb, B., Frolich, R.M., 1993. Satellite radar interferometry for monitoring ice sheet motion: application to an Antarctic ice stream. Science, 262:1525-1530.
[3]. Kwok, R., Fahnestock, M.A., 1996. Ice sheet motion and topography from radar interferometry. IEEE Transactions on Geoscience and Remote Sensing, 34(1):189-200.
[4]. Massonnet, D., Rossi, M., Carmona, C., Adragna, F., Peltzer, G., Felgl, K., Rabaute, T., 1993. The displacement field of the Landers earthquake mapped by radar interferometry. Nature, 364:138-142.
[5]. Massonnet, D., Feigl, K., Rossi, M., Adragna, F., 1994. Radar interferometry mapping of deformation in the year after the Landers earthquake. Nature, 369:227-230.
[6]. Massonnet, D., Briole, P., Arnaud, A., 1995. Deflation of Mount Etna monitored by spaceborne radar interferometry. Nature, 375:567-570.
[7]. Amelung, F., Jonson, S., Zebker, H.A., Segall, P., 2000. Widespread uplift and 'trapdoor' faulting on Galápagos volcanoes observed with radar interferometry. Nature, 407:993-996.
[8]. Carnec, C., Massonnet, D., King, C., 1996. Two examples of the use of SAR interferometry on displacement fields of small spatial extent. Geophysical Research Letters, 23(24):3579-3582.

[9]. Kimura, H., Yamaguchi, Y., 2000. Detection of landslide areas using satellite radar interferometry. Photogrammetric Engineering & Remote Sensing, 66(3):337-344.
[10]. Amelung, F., Galloway, D.L., Bell, J.W., Zebker, H.A., Laczniak, R.J., 1999. Sensing the ups and downs of Las Vegas: InSAR reveals structural control of land subsidence and aquifer-system deformation. Geology, 27(6):483-486.
[11]. Tesauro, M., Berardino, P., Lanari, R., Sansosti, E., Fornaro, G., Franceschetti, G., 2000. Urban subsidence inside the city of Napoli (Italy) observed by satellite radar interferometry. Geophysical Research Letters, 27(13):1961-1964.
[12]. Strozzi, T., Wegmuller, U., Tosi, L., Bitelli, G., Spreckels, V., 2001. Land subsidence monitoring with differential SAR interferometry. Photogrammetric Eng. & Remote Sensing, 67(11):1261-1270.
[13]. Agudo, M., Biescas, E., Monserrat, O., Martínez, J., Crosetto, M., Herrera, G., 2005. ¿Cómo medir las deformaciones del terreno con teledetección radar? 6ª Semana Geomática, Barcelona, 8-11 Febrero 2005.
[14]. Baarda, W., 1968. A testing procedure for use in geodetic networks. Netherlands Geodetic Commission, Publications on Geodesy, 2 (5), Delft (Holland).
[15]. Moritz, H., 1978. Least-squares collocation. Rev. Geophys. Space Phys., 16, 421-430.
[16]. Dermanis A., 1984. Kriging and collocation: A comparison. Manuscripta Geodaetica, 9(3), 159–167.